ESCUELA TÉCNICA SUPERIOR DE INGENIERÍA DE TELECOMUNICACIÓN
UNIVERSIDAD POLITÉCNICA DE CARTAGENA

Proyecto Fin de Carrera

Development of Pre-processing Methods for Attenuation Correction Algorithms in Small Animal PET/MR Imaging

AUTOR: Diego Vivancos Gallego
DIRECTORES: Sibylle Ziegler, Ph.D.
Prof. Nassir Navab, Ph.D.
Marc Huisman, Ph.D.
Wolfgang Wein, Dipl. Inf.
CODIRECTOR: Dra. Magdalena Rafecas López

DICIEMBRE / 2004

Diplomarbeit

Development of pre-processing methods for attenuation correction algorithms in small animal PET/MR imaging

In collaboration with Nuklearmedizinische Klinik and Chair for Computer Aided Medical Procedures

Technische Universität München

Diego Vivancos Gallego
serru@ono.com

Supervision: Sibylle Ziegler, Ph.D. (NMK)
Prof. Nassir Navab, Ph.D. (CAMP)
Marc Huisman, Ph.D. (NMK)
Wolfgang Wein, Dipl. Inf. (CAMP)

Date: 20th December 2004

Abstract

Signal processing includes a wide variety of signals, such as $2D$ and $3D$ images. New techniques of signal processing are widely accepted in medicine, where inter-modality techniques are today unquestionably required for its use in diagnosis. Tumor or Alzheimer detection requires the use of new radio-pharmaceutical tracers that should be tested in small animals, such as mice or rats. Medical techniques for diagnosis as Magnetic Resonance Imaging and Positron Emission Tomography provide complementary information about diseases in a patient or animal. Before inter-modality integration, many processes are required. In this work pre-processing methods are developed, such as registration and segmentation. After pre-processing an attenuation map is derived, that can be used to perform an attenuation artifact-free reconstruction of Positron Emission Tomography images of small animals.

Resumen

El procesado de señal incluye una gran variedad de señales, tales como imágenes $2D$ y $3D$. El rápido desarrollo de este tipo de procesado de señal tiene aceptación en la medicina, donde actualmente técnicas multi-modalidad son de incuestionable validez en el diagnóstico de enfermedades. La detección prematura de tumores o Alzheimer requiere el uso de nuevos compuestos radioactivos que deben ser probados en pequeños animales como ratones y ratas. Técnicas para el diagnóstico como Resonancia Magnética y Tomografía por Emisión de Positrones proporcionan información complementaria acerca de una enfermedad en pacientes o animales. Antes de la integración multi-modalidad, varios procesos son necesarios. En este trabajo se han desarrollado métodos de pre-procesado, tales como registrado y segmentación para obtener un mapa de atenuación, que pueda ser usado para realizar una reconstrucción libre de artefactos para Tomografía por Emisión de Positrones aplicada a pequeños animales.

Preface

About this work This document is my *"Proyecto final de carrera"* for the degree *"Ingeniero Superior de Telecomunicación"* at the *"Universidad Politécnica de Cartagena"* (UPCT). All the experimental work was done at the Nuklearmedizinische Klinik of the Klinikum rechts der Isar, supported by the Chair for Computer Aided Medical Procedures at the Fakultät für Informatik at the Technische Universität München (TUM). I was working from March to August performing some experiments and programming software to develop pre-processing methods in small animal Positron Emission Tomography for attenuation correction algorithms based on Magnetic Resonance data.

Acknowledgments First, I am very grateful for the help that Magdalena Rafecas gave me before arriving to München, and for her support during her stay in the Klinikum. Thanks to Wolfgang Wein for help me not only with my report and the informatic side of the project, besides to find a room in München (it was not easy). Thanks also to Marc Huismann for helping me with the experiments and with the report, and every day with his presence in our work room. In the Nuklearmedizinische Klinik thanks to all the following people headed by Dr. Sibylle Ziegler: Magdalena Rafecas, David McElroy, Mary Spilker, María José Martínez, Virginia Spanoudaki, Marc Huismann. In the Fakultät für Informatik thanks to all the following people of the Chair for Computer Aided Medical Procedures headed by Prof. Nassir Navab: Wolfgang Wein, Darko Zikic.
Many thanks to Prof. Fernando Cerdán Cartagena for help me with the academic issues, and thanks also to the International Relations Department in my university. Finally thanks to all that people that made me feel good during my stay in München. Congratulations!

Contents

List of Figures

List of Tables

Chapter 1

Introduction

1.1 Motivation

Imaging technologies are originally developed for use in human medical diagnosis. In this report we will consider techniques adapted to imaging small animals such as mice and rats. New radiopharmaceutical tracers applied in kinetic studies, such as tumor and Alzheimer detection, should be tested in small animals. Actually, a profuse research in this field of investigation is made, from the medical and engineering points of view.

After applying to a patient or animal a specific tracer, positron emission tomography (PET) scanners detect the concentration of activity in a certain area of interest. The basic principle of PET establish correspondence between the amount of photon coincidences detected in the scanner and the concentration of activity in this area. The photons are attenuated as they pass through matter. Therefore typical reconstruction artifacts are shown in the final images. This is due to a depression of activity in the areas that are more in the center of the body. Techniques to develop the correction of PET for attenuation is the aim of this report. Then an artifact-free reconstruction of PET can be obtained and more accurate images of PET can be used in diagnosis. In this report this techniques comprise registration and segmentation methods based on magnetic resonance (MR) imaging.

PET and MR are prominent examples of functional and anatomical imaging modalities, respectively. The imaging concepts of PET and MR are quite different. The complementary nature of information provided by them are useful in conjunction. PET images may completely lack any anatomical information but are able to provide functional information. This information could be, for instance, the cerebral blood flow or the density of a receptor in a certain area. On the contrary MR shows tissue types and, thus, provides information about anatomy of structures.

More and more, the amount of data is increased due to improvements in resolution and speed of each successive generation of acquisition systems. This combined with significant advances in computer networks and hardware, offers the possibility to store the data in new mediums and to work with high computational-intensive algorithms, while still reducing the time to present the results. These algorithms are applied in registration and segmentation methods.

The main aim of registration is to provide an exact correspondence between the voxels

of different modalities (PET-MR), as far as possible in an automated manner.

Another important step is segmentation, that detects the different tissues that compound the MR image. The attenuation map provides the amount of absorbed photons depending on the tissue that the gamma rays go through for each voxel in PET volume. As a result, using the attenuation map in the PET reconstruction process, quantitative artifact-free PET data are obtained.

1.2 About Acquisition Methods

In vivo imaging is an important tool in medicine for diagnosis and treatment of patients. Internal organs can be viewed with precision and safety. The first medical tomography technique was based on the x-ray attenuation coefficient. Cormack and Hounsfield received the Nobel Prize in 1979 for the "development of computer assisted tomography" [1]. Subsequently, tomography was extended to other fields as nuclear medicine and magnetic resonance. In nuclear medicine the interest is in reconstructing a PET image of radioactive isotope distribution within the human body. In magnetic resonance, the imaging principle is based on the magnetic properties of the object.

Multi-modal image registration integrates the complementary information available in different modalities. The most used acquisition techniques are: X-ray Computed Tomography (CT) and Magnetic Resonance (MR), that provide anatomical information; and Positron Emission Tomography (PET) that supplies functional information.

CT is based on forming a projection by combining the line integrals that represent the total attenuation of x-rays beams. By using reconstruction algorithms a three dimensional reconstruction is made. Scanning methods can give different quality of the reconstructed image, for example helical and multi-slice CT. The reconstruction grid, photon energy, detectors, speed, number of samples and number of projections can introduce significant changes in the final quality of the acquired image.

MR applies electromagnetic radiation. Each pulse sequence corresponds to a specific image contrast. In modern MR systems multiple planes (transverse, coronal, sagittal, and oblique orientation) can be acquired. This permits a good imaging of the organ, or particular region of interest. The main advantage is the higher spatial resolution compared with PET images, resulting in detailed anatomical information.

PET employs the advantages of the development of new radiopharmaceutical tracers. The tracer is labeled with an isotope which emits positrons. Such isotopes may be available from some atoms like oxygen (as ^{15}O, $t_{1/2} = 2.05\ min$), carbon (as ^{11}C, $t_{1/2} = 20.4\ min$), nitrogen (as ^{13}N, $t_{1/2} = 10\ min$) and fluorine (as ^{18}F, $t_{1/2} = 109.7\ min$), where $t_{1/2}$ is the half-time life of the given isotope. Positron-emitting radionuclides are produced under controlled laboratory conditions in particle accelerators. The most widely used tracer is $^{18}F\text{-}FDG$ (2-[^{18}F]-$fluororo\text{-}deoxy\text{-}D\text{-}glucose$), in which the isotope is bonded to glucose. With this substance the consumption of glucose in the human brain can be determined, or the presence of a tumor can be proven in oncological studies. Actually there is many research in PET instrumentation and reconstruction algorithms, as well as in the physical field as from the electronic point of view. For example new efficient radiation detectors are developed. The major problem of PET is its cost. The short

half-life of most positron emitting isotopes requires an on-site cyclotron. Furthermore, reliability in tumor detection can be improved by image registration with CT or MR.

1.3 About Registration

In the past, software registration [2] was limited by the image transfer between mediums and computer networks. Furthermore, the profusion of poorly validated algorithms hampered software registration. With the arrival of new developments in hardware, new and robust algorithms have become available, especially for the case of non rigid body registration. Maintz and Viergever [3] have classified the medical image registration methods according to nine criteria. The most important of them for this report are introduced:

- **Dimensionality**. The data sets to be aligned can be three-dimensional (3D), though applications of 2D-3D, as well as 2D-2D registration have been described as different spatial registration methods. In this report the problem is 3D-3D.

- **Nature of registration basis**. As for the nature of registration methods can be divided in extrinsic, relying on artificial objects attached to the patient; intrinsic, based only on the information that the image contains itself; and non-imaged, that works with parameters foreign to the images characteristics.

  The extrinsic methods require that the external objects should be well visible in the imaging process between different modalities. Often the nature of this registration is rigid. An extrinsic registration method has been developed in this work.

  The intrinsic methods can be based on landmarks, with a limited set of identifiable points; segmentation, aligning certain pre-segmented structures; or working with voxel properties, computing the values of each voxel. An intrinsic registration method has been also developed in this work.

  Finally the non imaged are based on calibration methods within the scanners by establishing the same physical location.

- **Nature of transformation**. Registration requires the determination of a transformation that can be applied to one image (referred to as the floating image) to bring it into alignment with the other image (referred to as the reference image).

  Rigid-body transformation preserves the distance between two given points in the body, irrespective of how the body is transformed. Therefore, the only permissible transformations between the two image sets are rotations and translations, applied to the complete data set. It requires six parameters: three rotations and three translations. To represent zooming, an additional parameter representing global scale can be added. However, in most cases the relative voxel size and aspect ratio of the image sets can be determined prior to registration. Subsequently, any differences in scale can be adjusted before actual registration. As a general rule, the speed of registration is improved by lowering the number of parameters, but probably the accuracy is not improved.

However, some fields of image registration requires non-rigid body registration. Examples include: brain images of different individuals, matching a brain study to an anatomical atlas, internal organs that change its shape such as the heart. In these cases the distance between corresponding voxels is not the same all the time. It is not trivial to registrate these images that correspond to the same region of interest.

In our case only rigid registration is required and finally we can conclude saying that non-rigid validation is extremely difficult and continues to be an area of active research.

- **Subject(s) and modalit(y/ies) involved**. In [4] four basic classes are distinguished based on the subject(s) and modalit(y/ies) involved in registration:
  - Intra-subject, intra-modality: alignment of studies in the same subject acquired in the same modality.
  - Intra-subject, inter-modality: alignment of studies in the same subject across different modalities.
  - Inter-subject, intra-modality: alignment of studies of different subjects in the same modality.
  - Inter-subject, inter-modality: alignment of studies of different subjects across different modalities.

According to [5] and taking into account the criteria commented before, an image registration algorithm comprises a number of decisions and processes, summarized below:

1. Choice of transformation: rigid-body with or without scaling, non-rigid; if non-rigid, type and number of parameters.
2. Choice of the measure of alignment (or misalignment) and the method of optimizing this measure.
3. A decision on which will be the target image and which the source image to be transformed to the target.
4. A pre-processing step to delineate corresponding structures, transform intensities, and scaling, if necessary.
5. Computation of the transformation by optimization of the measure of alignment. For this, an optimization algorithm should be selected.
6. Transformation of the source image, or discrete points in the source image, to the coordinate system of the target image.
7. Viewing and manipulation of the results.

Determining the necessary transformation requires an iterative search for every registration method. This process maximizes a measure of similarity between the transformed floating image and the reference image or, in other words, a measure of error for the alignment should be minimize. This is usually achieved by using an iterative, automatic optimization algorithm.

1.4 About Segmentation

Segmentation of $3D$ volumes means partitioning of voxels into different regions grouping to those ones that belong to the same structure. For example, segmentation is required to differentiate the most important physical entities: brain, bone and background. To know to what region each voxel belongs, some voxel properties have to be computed. These properties can be proximity, spatial position, texture and intensity value. Segmentation can be integrated in many processes: registration, pattern recognition, etc. Depending on the segmentation class it may be single contrast or multi-spectral. Single contrast generates simples structures, while multi-spectral works with many different images that contain distinct information corresponding to the same region of interest. Other classifications are supervised and unsupervised methods. Supervised methods require operator input at a given moment during the segmentation process. Unsupervised methods are automatic since the result is not dependent on the operator.

Although a simple approach could be thresholding an image (point-based segmentation), spatial information is required to know proximity and connectivity properties. Taking advantage of this kind of information region-based segmentation techniques such as region-growing and region merging can be used to select regions of interest among other objects present in a $3D$ volume. There are four classical approaches:

- **Thresholding techniques**. These are based in threshold values extracted from the intensity histogram. All voxels whose value are between two values belong to the same region.

- **Edge-based methods**. Find the transitions between intensity values as a gradient information. The image obtained has the boundaries or edges of a specific object.

- **Region-based methods**. An homogeneity criterion is applied and the regions are assigned accordingly.

- **Hybrid methods**. A combination between the methods commented before, for example edge and region methods.

A not very recent classification of segmentation methods is shown in [6]. In this project only 3D region-based methods have been used to segment MR images.

Automatic methods are complicated when no interaction with an operator takes place. Other problems can be the computation time and the accuracy after segmentation. These problems have not been solved yet and this is a very active research area. Therefore, the most simple way of interaction with segmentation methods is to select a threshold. A good description of $3D$ segmentation algorithms is found in [7].

1.5 About Attenuation Map

PET images are based on the emission of a distribution of positrons within a living body, which results from the decay of a radioactive substance previously injected to the patient or animal. Raw PET data correspond to the detection of two 511 keV gamma

rays resulting from the annihilation of the positron with an electron of the tissue. Some of the emitted gamma rays never reach the detector but are absorbed within the body due mainly to the Compton scattering. The amount of absorbed photons depends on the tissue that the radiation is going through, and on the length of the radiation path through each tissue. Therefore, a so called attenuation map is needed to obtain quantitative data. One way to obtain a bias free attenuation map proceeds via segmentation of co-registered MR data.

Each of the imaging methods has different values of noise versus inaccuracy (bias). For instance, PET has the relative lowest bias but the relative highest noise, CT scanners have insignificant noise and bias, and MR can have bias but relatively no noise. The use of attenuation correction results in a more accurate image after reconstruction. Anyway, careful inspection of the corrected data should be made, in the case that artifacts or noise are significantly present. A post-analysis of the acquisitions with and without attenuation correction is desirable.

Attenuation correction has been developed for many PET/CT scanners [8, 9]. The PET/MR case [10], and the PET/MR small animal are more specific [11]. In this case the MR and PET techniques are not integrated in the same scanner. Therefore it is not possible to do an automatic correction. The two data sets should be treated apart.

1.6 Outline of this project

The algorithm used for attenuation correction of data obtained from MR and PET to generate an attenuation map is shown in the figure 1.1. The basics steps consist on the following:

1. Acquire PET and MR data for the phantom. (see chapter 2)
2. Preliminary PET reconstruction.
3. Pre-processing of each data set according to algorithm requirements. (see chapter 3)
4. Run the optimization process finding the maximum similarity measurement or by minimizing the alignment error.
5. Record spatial transformation matrix for MRI.
6. Apply same spatial transformation to original MR images.
7. Segment the MR images to three regions: air, water and activity. (see chapter 4)
8. Obtain the segmented MR-based attenuation map for PET. (see chapter 5)
9. Attenuation correction using the segmented MRI-based attenuation map.
10. Final 3D PET reconstruction.

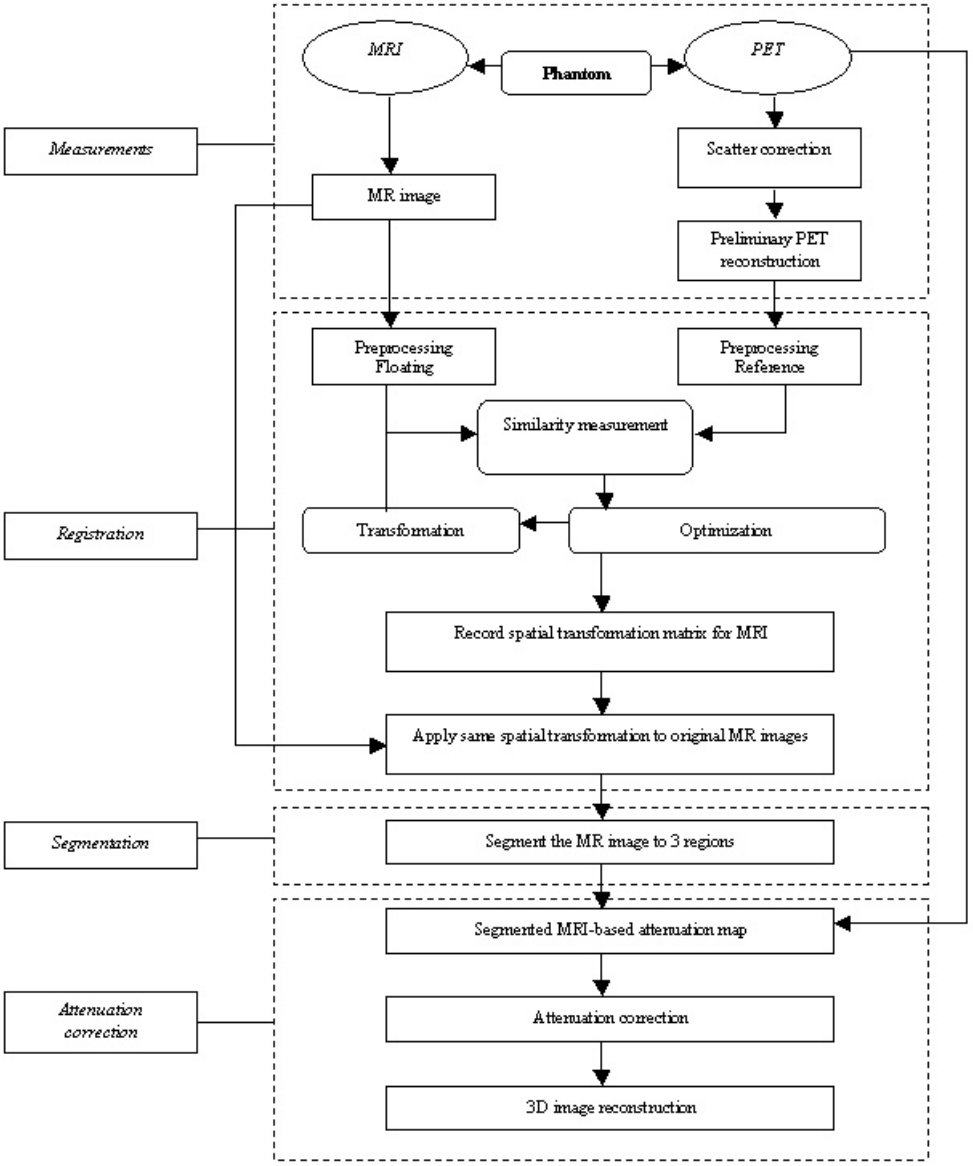

Figure 1.1: Flow-chart of the algorithm with the different steps to generate an attenuation map from segmented MR images

In total two full data measurements are made in the small animal PET scanner (MADPET-I) (see reference [12]), that is at the Nuklearmedizinische Klinik of the Technische Universität München. That scanner is a high resolution prototype based on the individual readout of small LSO scintillation crystals coupled to avalanche photo-diodes. Due to the particular geometry of MADPET-I, consisting of six detector modules mounted on an octagonal support, rotation of the scanner is required. The acquired data correspond to a 2D slice of the object or animal under study. To obtain a 3D image, several measurements are needed, and post-compensation for the attenuation decay of each slices are required.

A new small animal PET system, the *Mosaic* developed by Phillips, is installed at the Nuklearmedizinische Klinik, and the final work is performed with this scanner.

In addition to these small animal systems, a clinical magnetic resonance MR device is available for diagnostic imaging. A first acquisition is made in PET-CT but finally only the MR is used. The CT was discarded because the clinical PET/CT scanner resolution is not good enough and provides high radiation doses for the small animals.

Two algorithms are used to register the volumes, the first is a extrinsic method based on multiple orthogonal 2D projections. Along each orthogonal axis, 2D images are projected from the 3D volumes as maximum intensity projection (MIP). After applying a Canny edge detector in each projection, in one of them a circle is extracted as specific feature by Hough Transform. The discrepancy between the floating volume and the reference volume is measured by the Distance Transform applied to the three binary projections. The second is a intrinsic method, the Mutual Information (MI) based method. The two data sets are considered as random variables and information theoretic techniques are applied. Differences concerning efficiency and time computation are observed.

Two algorithms are applied to segment the MR data. These algorithms are region-based segmentation techniques: seeded region growing and region merging. They take account spatial information, such as proximity and connectivity. Different results were obtained depending on the segmentation automation.

In the following chapters the physical phenomenons and the algorithmic and software issues are described. In chapter 2 the different modalities under study PET and MR are introduced from the physical point of view. Chapter 3 comments all the aspects related to registration as well as interpolation, and the step by step development of each algorithm (2D orthogonal projections vs Mutual Information). To obtain the attenuation map, segmentation is required, all these issues are commented in chapter 4. A summary to develop an attenuation map based on MR segmentation is described in chapter 5. Chapter 6 contains the results for the data acquisition. The algorithm results are in chapter 7. The conclusions and future work are in Chapter 8. Further information about the algorithm results (appendices A and B) and glossary (appendix C) are at the end of the report.

Chapter 2

Equipment: PET and MR

2.1 Overview

Radiation can be classified according to its behavior: it can be an electromagnetic wave or a particulate. Ionising radiation has sufficient energy described as to remove electrons from atoms, thus causing ionisation. This is restricted to high-energy electromagnetic radiation (X and γ radiation) used for medical imaging, and charged particles (α, β^-, β^+). Examples of non-ionising radiation include light, radio, and microwaves (see figure 2.1).

The amount of energy is determined by the wavelength (λ) of the radiation. Human senses are capable of detecting some forms of electromagnetic radiation, for example, thermal radiation, or heat, ($\lambda \approx 10^{-5}\ m$), and visible light ($\lambda \approx 10^{-7}\ m$). Depending on the material the energy of the radiation can be absorbed to a different degree: light can be stopped by paper, whereas radiation with longer wavelength (radio waves) or higher energy (γ rays) can penetrate the same paper.

X rays are electromagnetic radiation produced within an atom, but outside of the nucleus. Characteristic X rays are produced when orbital electrons drop down to fill vacancies in the atom after an inner shell electron is displaced. As the outer shell electron drops down to the vacancy, it gives off energy and this is known as a characteristic X ray. The energy of the X ray is determined by the difference in the binding energies between the electron levels. X rays generally have energies in the range of $\approx 10^3$-$10^5\ eV$.

Gamma rays are electromagnetic radiation emitted from the nucleus after a spontaneous nuclear decay. X and γ rays are indistinguishable after they are emitted from the atom, and only differ in their site of origin. Gamma ray emission is determined by the difference in energy levels between the initial and final energy level within the nucleus. γ rays generally have energies in the range of $\approx 511\ keV$.

2.2 Magnetic Resonance

2.2.1 Basic Principles of MR Imaging

In [13] and [14] we have reference for this phenomenon which I would like to summarize here.

In 1946 Bloch and Purcell made the first experiments, as a result MR was used successful in analytical chemistry and biochemistry. Clinical applications of MR resulted from work by Lauterbur who shows the possibility of spatial localization of the MR signal by using magnetic field gradients. The first images of humans were obtained in 1977. From the 1980's innovations were made on MR scanners, and since then they have been developed into a powerful medical diagnostic technique.

A strong magnetic field (B_0) aligns the nuclear spins (or magnetic angular momentum) of certain atoms. This alignment results in an orientation either parallel or anti parallel to the main magnetic field. Orientation of the magnetic dipole moment parallel to the external field represents the state of lower energy. The distribution between low and high, energy states depends on the strength of B_0 and the temperature. The distribution is given by the Boltzmann equation (see equation 2.1), where n^- and n^+ are numbers of nuclei in the two states, k is the Boltzmann constant, ΔE is the energy difference and T the temperature.

$$\frac{n^-}{n^+} = e^{\frac{-\Delta E}{kT}} \tag{2.1}$$

The magnetic moment of the nuclei precess around the axis of B_0 with a frequency (υ_0), called the resonance or Larmor frequency, which is directly proportional to B_0 (see equation 2.2), where γ is the gyromagnetic ratio.

$$\upsilon_0 = \gamma \cdot B_0 \tag{2.2}$$

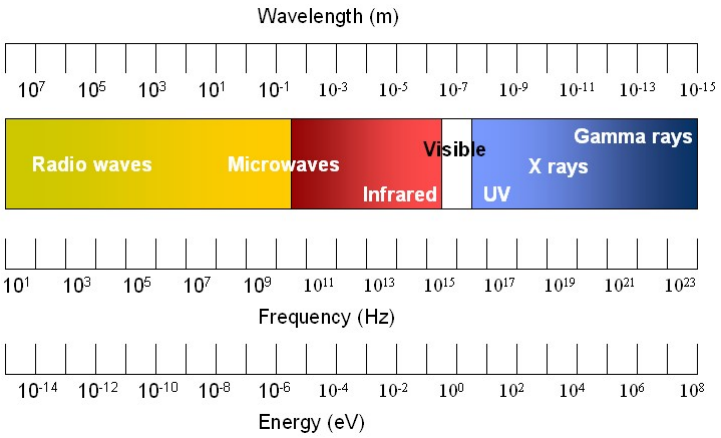

Figure 2.1: Electromagnetic spectrum: relationship between energy, frequency and wavelength

For ^1H, its spin quantum number of 1/2 means that the nuclei have two energy states corresponding to parallel or anti parallel orientation. It is the nucleus of choice for magnetic resonance due to its natural abundance in the body, and its high sensitivity of the corresponding MR signal (42.58 $MHz/Tesla$) provides a good contrast for tissues.

The energies involved in MR are non-ionizing and the magnetic field are typically in the range of 0.3 to 3 $Tesla$. By applying adequate pulse sequences the desired contrast is obtained. When a RF energy is applied to a nuclei at the Larmor frequency, their magnetic orientation changes (see figure 2.2). A net magnetization, represented by a vector M_0 results. Depending on the duration and strength of the RF pulse a flip angle determines the amount of rotation. Common flip angles are 90° and 180°, where the magnetization is rotated into a plane perpendicular to B_0 and is inverted or aligned anti parallel to B_0, respectively .

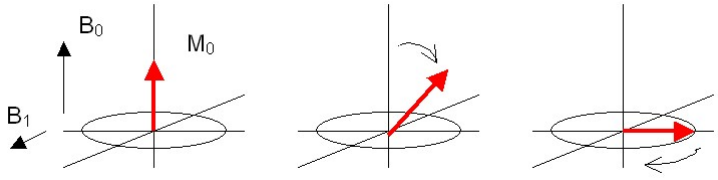

Figure 2.2: Application of the alternating RF excitation to spins. B_1 represents the 90° pulse and B_0 represent the main field. After the RF pulse induced rotation (first two diagrams) the magnetization is used for MR imaging

2.2.2 Relaxation Phenomenon

When the RF excitation stops, a process called relaxation, returns the magnetization to its original equilibrium. Once the magnetization is deflected, the RF field is turned off and the magnetization returns to the direction of B_0. This precession induces a current in the RF coil according to *Faraday's Law of Induction*. The measured voltage, called free induction decay (FID) (see figure 2.3), decays in an exponential manner.

The relaxation process is characterized by two time constants, $T1$ and $T2$. The capability to produce detailed MR images depend on this time constants and on the physical and chemical characteristics of the tissues.

The spin-lattice relaxation time ($T1$) is due to the dissipation of the excess of energy absorbed in the stimulation to the lattice. In order to accomplish an effective transference of energy to the lattice, it must fluctuates at the *Larmor frequency*.

To understand $T1$ relaxation we can explain the phenomenon in this way: the equilibrium state M_0 is supposed to be oriented along the z-axis. A 90° RF pulse rotates M_0 into the transverse plane so that M_z is now equal to zero. $T1$ characterizes the exponential return of the M_z magnetization to M_0. To measure $T1$, an inversion sequence of a 180° RF pulse followed by a delay is applied, this delay is the inversion time TI (see figure 2.4).

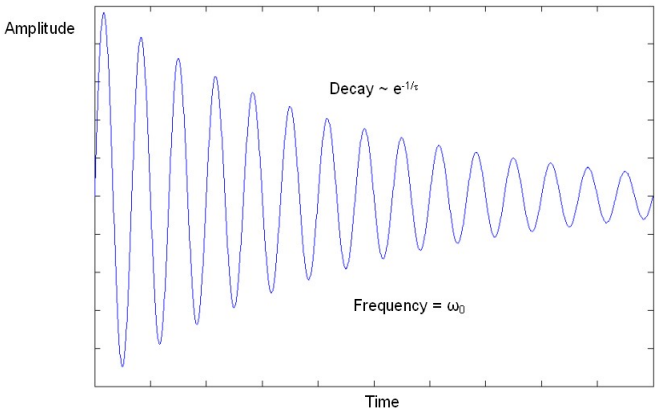

Figure 2.3: The free induction decay (FID) is due to absence of applied magnetic field gradients, after the RF field has been turned off

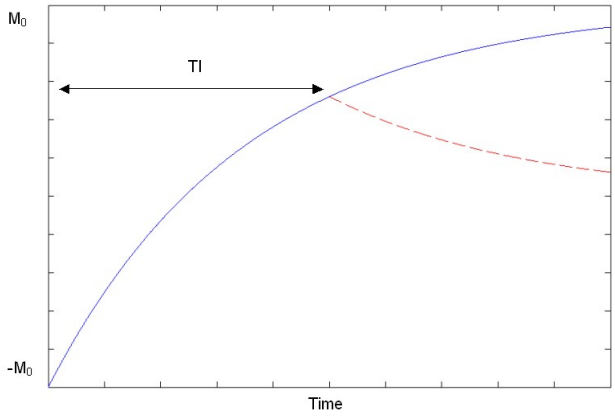

Figure 2.4: Spin-lattice relaxation ($T1$). An initial 180° RF pulse flips the magnetization along z axis, then the magnetization comes back to the equilibrium state with a time constant $T1$. Finally after TI inversion time a 90° pulse is applied

The spin-spin relaxation time ($T2$) is due to exchange of energy between nuclei. After an RF pulse the spins are in phase, but because of natural processes they lose their phase coherence, as a consequence the transverse magnetization M_T decays to zero exponentially. What is more, other processes also cause the dephase, then, when the natural processes and magnetic imperfections contribute, the decay is denoted $T2^*$. Both $T2$ and $T2^*$ are smaller than $T1$.

The spin-echo pulse sequence corrects the transverse decay of the field inhomogeneities. It consists in a 90° followed by a 180° RF pulses, and a subsequent signal acquisition (AQ).

$$S(90^\circ) \rightarrow \tau \rightarrow S(180^\circ) \rightarrow \tau \rightarrow AQ \tag{2.3}$$

Some time after applying the initial 90° pulse the 180° is applied and the spins flip in a mirror position. At a time τ the fast spins catch up with the slow spins and the spin echo is created (see figure 2.5). The total period time between the 90° sequence and the echo is called echo time $TE = 2\tau$.

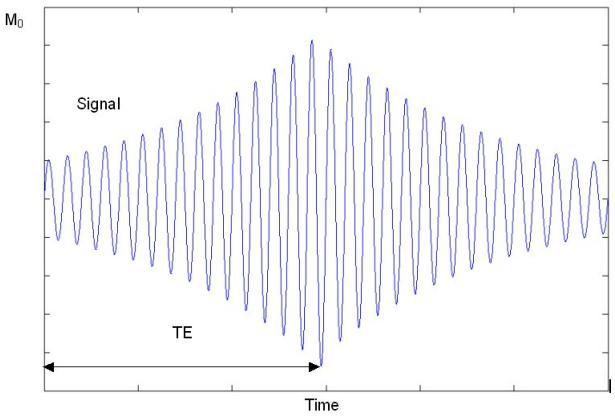

Figure 2.5: Spin echo sequence. The amplitude of the signal is modulated by $T2$ relaxation of the spins. The amplitude depends on the echo time TE

Different contrast is given by the selection of appropriate echo time (TE) and repetition time (TR). The tissue contrast depends on the times $T1$ and $T2$. This produces a differentiation in the images of the same anatomy. The main magnetic field is altered along a selected direction, as a result linear magnetic gradients are added and the resonance frequency varies with the location, providing the information necessary to make an image. The steps slice selection, frequency encoding and phase encoding determine the excitation and localization of the spins. These steps are required to obtain a two dimensional image.

2.2.3 Scanner Errors and Factors Affecting the MR Image

Variations in magnetic susceptibilities due to the class of material (diamagnetic, paramagnetic, super paramagnetic and ferromagnetic) within a voxel, produce local inhomogeneities in the magnetic field. These local inhomogeneities produce dephasing and, as a result, signal loss and image distortion are present in the final MR image.

The magnitude of distortion generally varies in the MR image space. It can be easily measured using phantoms (see section 6.2), normally it depends on the design and performance of the scanner.

Three possible causes determine a geometric distortion based on field inhomogeneity: imperfection of the field generated by the magnet, spatial variations in the magnetic susceptibility and eddy currents induced in the conducting structures of the scanner. These effects cause local variations in the resonance frequency and are inversely proportional to gradient strength. Then the distortion is reduced by increasing the gradient strength, which is equivalent to increasing the bandwidth per pixel.

Intensity can be also due to inhomogeneity in the RF, for example in the same tissue different places appear with different intensity.

Fluctuations in the imaging gradient amplitudes could present errors in the voxel dimensions. The correction is based on registration methods that incorporate linear scaling factors to compensate the differences. One important problem to discuss is the signal non-uniformity due to RF inhomogeneity. It could be a problem for acquisitions with smaller RF coils.

On the one hand several post-processing methods can be used to achieve the correction, but on the other, the problem can be resolved in the registration step in two ways: correcting the images prior to registration, or using a registration method less sensitive to signal non-uniformity.

2.3 Positron Emission Tomography

2.3.1 Basic Principles of Positron Emission Tomography

Paul AM Dirac and Carl Anderson received the Nobel Prize in physics for their contributions to the investigations of positrons. Some literature talks about the PET phenomenon [15, 16].

The common form of nuclear medicine tracers consist of a radio-isotope bound to a chemical compound (usually glucose). After the tracer is administered (by inhalation or intravenous), a gamma camera detects the decaying of single photons. The camera normally is endowed with a lead collimator to limit the opening angle of the opposite photons emitted along parallel paths. Then, crystal scintillators convert high-frequency photons to visible light, and photo-multipliers determine the energy and position of each incident photon from the light distribution of the crystal.

Single-photon emission tomography (SPECT) was the first application of this technique. The gamma camera was rotated and the measured signal was corrected for attenuation. Finally the actual PET technology is developed.

Functional imaging is achieved with an initial introduction of the radioactive chemical compound. After waiting an appropriate time for the adequate distribution of it to the organs or regions of interest (approximately 30 minutes for $^{18}F\text{-}FDG$), the scan begins. When the radio isotope decays it emits a positron, which travels a short distance before annihilating with an electron. The energy of annihilation radiation is equivalent to the rest mass of the electron and positron, if the annihilation occurs in the spin 0 state, then two high energy 511 keV photons are given off at close to 180° opposite directions (see

figure 2.6). On the contrary if the annihilation occurs in the spin 1 state, three gamma photons are created. Fortunately this is less probable ($< 1\%$ probability). The property of colinearity is exploited in PET, allowing to find a true coincidence when the photons are detected between a short time frame ($\approx 10ns$), because they are emitted at the same time.

The rate at which nuclei spontaneously decay is characterized by the half-life ($t_{1/2}$) of the radionuclide, which is the time that it takes for half of the unstable nuclei to decay. The number of atoms decaying function has an exponential behavior compared with time (equation 2.4). A_0 is the initial activity, and A_t is the current activity at a given time t with a decay constant λ (equation 2.5).

$$A_t = A_0 e^{-\lambda t} \tag{2.4}$$

$$\lambda = \frac{log_e(2)}{t_{1/2}} \tag{2.5}$$

The decay correction factor (F) (equation 2.6) can be calculated from the point in time of an instantaneous measurement to a reference time, where t is the time of the measurement and t_0 is the reference time. It can be used to compensate the different $2D$ slices obtained from PET.

$$F = e^{\lambda(t-t_0)} \tag{2.6}$$

The fundamental limitations of spatial resolution in PET take origin in the finite distance traveled by the positron before annihilation, and the resulting uncertainty in its localization. Therefore the best obtainable resolution is the so-called intrinsic resolution that is typically 5 mm.

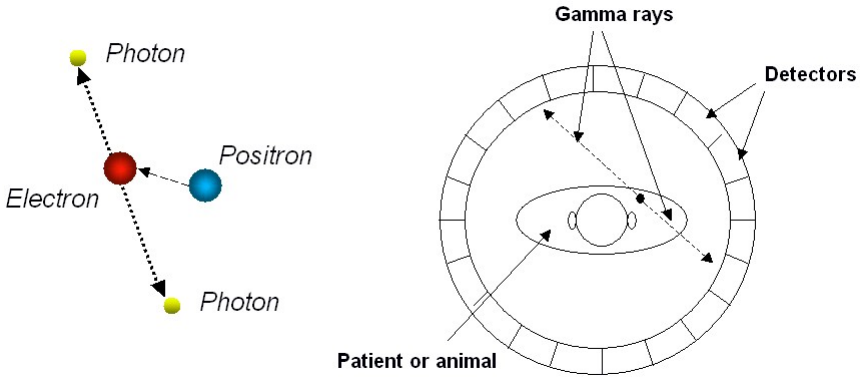

Figure 2.6: Annihilation phenomenon, resulting two gamma rays (511 keV) emitted under an angle of $180° \pm 0.25°$

2.3.2 Interaction of Radiation with Matter

Gamma photons interact with matter, and this interaction takes the form of an energy transfer. There are three basic interactions: photoelectric effect, Compton effect and pair production.

The photoelectric effect is an interaction in an atom of photons with inner shell electrons. All the energy of the photon is transferred to the electron. Some energy is transferred in form of kinetic energy, and the remaining is used to overcome the binding energy of the electron. This phenomenon occurs at energies less than approximately 100 keV, therefore it is important for low-energy radionuclides, and has not too much impact at 511 keV.

Compton scattering emerges from the interaction between a photon and a loosely bound orbital electron. The loosely connection of the electron to the atom makes it practically free. The band of energies where this effect predominates is approximately from 100 keV to $\approx$ 2 MeV.

The maximum energy loss is at 180°, then the photon is back-scattered. Compton scattering is not equally probable at all energies or scattering angles. It is the main cause of attenuation in the energy that PET works.

Pair production consists on the spontaneously conversion of one electron with energy greater than 1.022 MeV, to an electron and a positron in order to conserve the charge in the vicinity of a nucleus. The probability increases with the energy, this probability is approximately 60% at 10 MeV.

All three basic interactions and their effects are shown in figure 2.8.

2.3.3 Attenuation and Scattering of Photons

Photons interact in terms of scattering cross sections (σ). The sum of the cross sections for all the individual processes give us the total scattering cross section. These processes

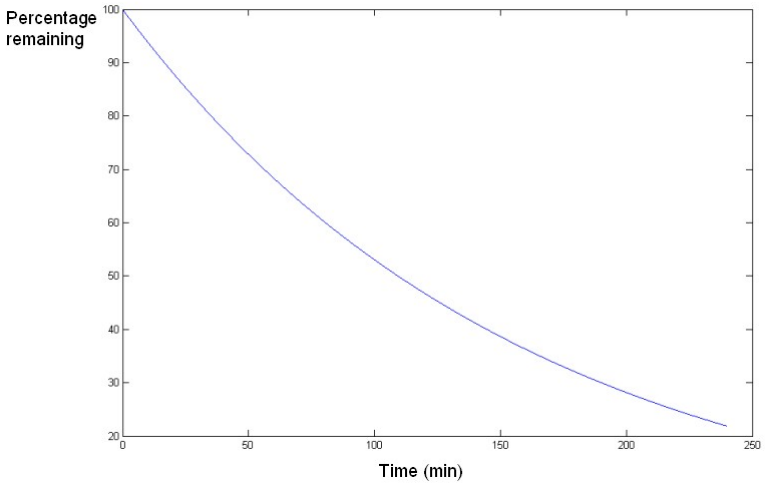

Figure 2.7: Decay of ^{18}F ($\lambda = 6.33 \times 10^{-3}\ min^{-1}$) during four hours (240 minutes)

are: photoelectric effect (σ_{pe}), scattering (Rayleigh and Compton) (σ_{sca}), pair production (σ_{pair}), triplet production (σ_{trip}), and nuclear photoabsorption (σ_{nph}).

$$\sigma_t = \sigma_{pe} + \sigma_{sca} + \sigma_{pair} + \sigma_{trip} + \sigma_{nph} \tag{2.7}$$

The unit for total scattering cross section is $cm^2/atom$, or cm^2/g, it can be converted to a linear attenuation coefficient (μ_l) (see table 2.1) by multiplying by the density (ρ) of the material:

$$\mu_l(cm^{-1}) = \frac{\mu}{\rho}(cm^2/g)\rho(g/cm^3) \tag{2.8}$$

Taking into account that the main effect at the energy of annihilation 511 keV is Compton interaction, the photon changes its direction and loses part of the energy. For a collimated source of photons and detector, the attenuation relation for the intensity of photons with the distance traveled is shown in equation 2.9. Where I_x is the intensity measured after passing through a material of thickness x and attenuation coefficient μ, and I_0 is the unattenuated intensity.

$$I_x = I_0 e^{-\mu x} \tag{2.9}$$

The path described by both annihilation photons determines the line-of-response (LOR) ascribed to an event. Due to scattering, the LOR may not intersect the object at all (see figure 2.10). Therefore, in many cases the detectors assign a false LOR to the coincidence. Finally, attenuation measurements, taking into account the effects commented in this section, are required to develop the attenuation map. Then quantitative PET data can be obtained.

2.3.4 Radiation Detection

Radiation detectors linearly convert the energy of radiation in a certain quantity of energy to be measured as electrical signal. Then the integral of this signal is proportional

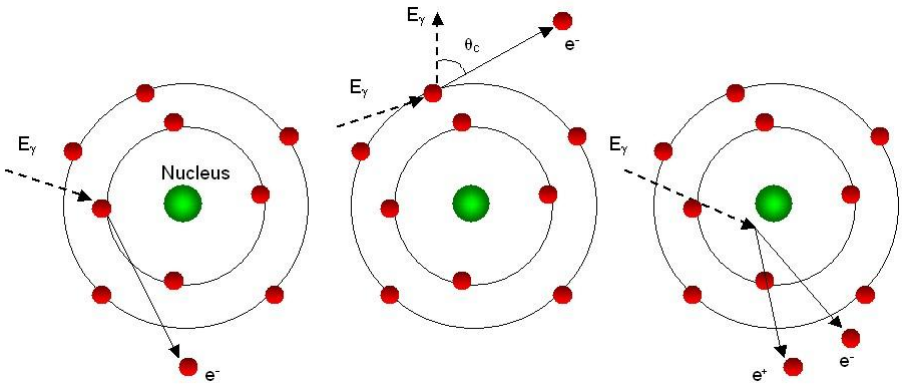

Figure 2.8: Photoelectric effect (Left), Compton scattering (Center), Pair production (Right)

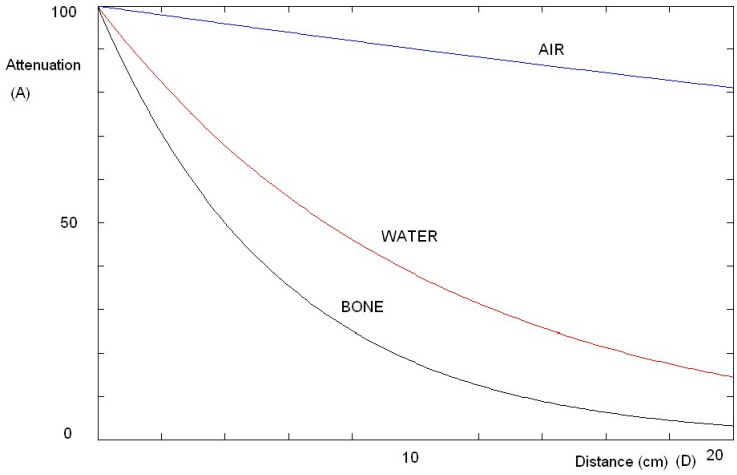

Figure 2.9: Percentage of attenuated photons through different tissues with the distance

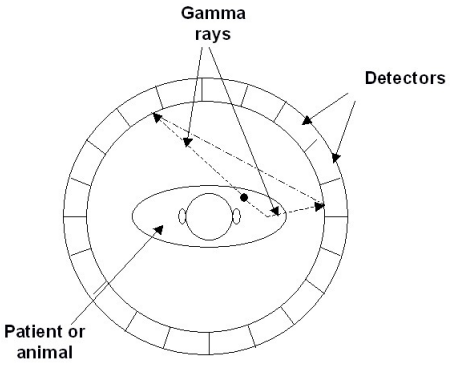

Figure 2.10: Scaterred photons in PET

Material	Density $(\rho)[g \cdot cm^{-3}]$	$\mu(511\ keV)[cm^{-1}]$
Adipose Tissue	0.95	0.092112
Air, Dry (Near sea level)	0.001205	0.00010498
Bone,Cortical	1.92	0.1732224
Breast tissue	1020	98.2362
Muscle, Skeletal	1.05	0.100779
Perspex (Lucite)	1.19	0.112
Pyrex, glass	2.23	0.194
Tissue, Soft	1060	101.7388
Water	1.0	0.09687

Table 2.1: Typical attenuation coefficients for different tissues (compiled from NIST data)

to the amount of energy previously deposited in the detector. Radiation detectors are divided in three main classes: proportional (gas) chambers, semiconductor detectors, and scintillation detectors.

A high electric field is applied within a proportional chamber. The radiation induced the ionisation electrons resulting in secondary ionisations. In the cathode a cascade of electrons is collected. The disadvantage of these detectors for use in PET is the low density of the gas, it means reduced stopping efficiency and poor energy resolution.

In solid-state semiconductor detectors, the incident radiation excites the electrons in the valence band and they migrate to the conduction band. By applying a electric field, a flow of charge is produced and light photons are emitted when the electrons return to the ground state. The stopping efficiency for 511 keV photons is low.

The scintillation detectors consist of an inorganic crystal (scintillator) which emits photons in the visible range of the EM spectrum (scintillation) as a result of an incident 511 keV photon. They provide the highest stopping efficiency, but the energy resolution is not as good as using semiconductor detectors. There are four important aspects to apply scintillators in PET: the stopping power, signal decay time, light output, and the intrinsic energy resolution. New organic scintillators have been developed, such as, $LuAp : Ce$, $Y_2SiO_5(YSO)$, $LuBO_3{:}Ce$, and others based on lead (Pb), tungsten (W) and gadolinium (Gd).

A photo-detector is used to measure the amount of incident energy. Two classes of photo-detectors are used: photo-multiplier tubes ($PMTs$) and semiconductor based photodiodes. Photo-multiplier has a good *signal-to-noise ratio* (SNR). Semiconductor photodiodes are actually used, these detectors are PIN diodes, where scintillation photons creates hole pair and, as a consequence a electrical charge can be measured. The low SNR, due to low amplification, made the avalanche photo diode (APD) a better option. Its internal amplification improves the gain and, therefore, a better SNR can be obtained.

To sum up, in PET a high stop efficiency and energy resolution are required. Because of this considerations the scintillation detectors combined with $PMTs$ are the most commonly used. Other configurations with APD can be also possible. A typical scheme for a detector module is shown in figure 2.11.

2.3.5 Timing Resolution and Coincidence Detection

The timing resolution represents the variability in the signal arrival times for an event. An event consists on the detection of two opposite photons corresponding to the same annihilation. Then two different times, $t1$ and $t2$, correspond with two different detection of single photons. Depending on the timing resolution of the detector, an appropriate value may be used to detect most of the valid coincidence events. For detectors with poor timing resolution a larger value is required for the coincidence window with length τ (see figure 2.12).

The fact that the two coincident photons can be emitted from anywhere within the (FOV), involves that different distances are traveled. Then taking into account the size of the PET scanner, an initial estimate of the time can be calculated. However, the coincidence timing window cannot be reduced to less than the difference in time of a emission in the edge of the scanner.

The typical problem associated with having a large coincidence window is the increased presence of random coincidences. The amount of random coincidences is proportional to $2\tau A^2$, where A is the activity presents in the FOV. The solution to decrease the random coincidences is applying a narrow window.

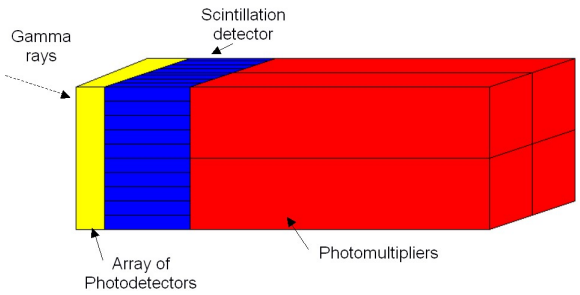

Figure 2.11: Multiple channel detector (array)

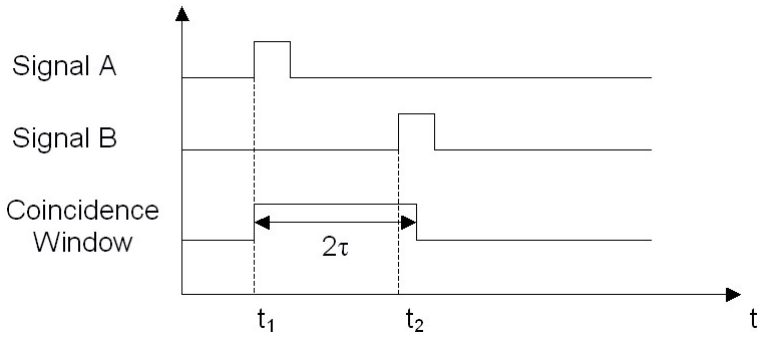

Figure 2.12: Detecting coincidence events in two detectors. Signal A results in the trigger or the first detector, similarly for signal B. A true coincidence is hardware detected

2.3.6 Reconstruction

The final aim of reconstruction is to recover the tracer concentration from the measurements. The reconstruction can assume deterministic data or statistical data, depending on the different techniques that are applied. The deterministic data technique ignores the noise, and measures the data by line integrals. For instance, a classic method could be *filtered-backprojection* (FBP). It is very simply but it has many problems, such as, negative values due to noise, the models for the detector response must be space-invariant, and the ramp filter accentuates high frequency noise. The statistical reconstruction [17] assumes Poisson independent distributions and evaluates estimator performance using basic properties, such as, bias and variance. The so called attenuation map can be also integrated in the reconstruction process.

2.3.7 Scanner Errors and Factors Affecting the PET Image

Registrating PET data with anatomical data, in our case MR data, has the fundamental problem of matching dissimilar data. To augment the similarity all the possibles sources of error must be minimized.

Examples of geometric and alignment errors include: poor alignment of the detectors, centre-of-rotation errors, non-uniform sampling and spatial distortion. The latter could be corrected prior to reconstruction, but in general the spatial resolution decreases towards the edge of FOV. This effect should be consider carefully. The centre-of-rotation errors should be carefully measured and corrected prior to reconstruction, or, on the contrary, the images can result in circular distortions. Finally, an accurate measurement of the reconstructed voxel dimension is needed.

Examples of physical errors include: intensity artifacts, spatial distortions and attenuation effects, that cause changes in the spatial distribution of the reconstructed signal. Without attenuation correction and taking account that attenuation is higher for photons originated in the center of the body, the final image can present decreasing artifacts. The correction may be applied before reconstruction in PET. A final source of error affecting the PET images is the reconstruction process. Artifacts produced in the process of reconstruction can come from extreme differences in the amount of activity between adjacent zones.

Chapter 3

Registration

According to section 1.3 we select a rigid transformation for our specific case. Two different methods based on similarity measures are described. Subsequently the optimization process is run.

3.1 Overview

The main objective of registration is to perform the correct alignment between images, checking the similarity measure in each iteration. This similarity reaches a maximum when the images are close to the best solution in the overlapping volume, or in other words, when the transformation parameters correspond to the real transformation. The choice of the similarity measure depends on the characteristics of each modality to register. It determines the robustness and flexibility of the algorithm. In this cases the general algorithm applied for each similarity measure is shown in figure 3.1.

A complete description about image registration can be found in [5]. Some mathematical concepts are useful to describe this process.

From a geometric point of view, registration is the transformation that establishes spatial correspondence between images. Then we denote the mapping $\mathbf{T}$, that transforms a position x_A in image A to a point x_B in image B

$$\mathbf{T} : x_A \mapsto x_B \Leftrightarrow \mathbf{T}(x_A) = x_B \tag{3.1}$$

The images have a limited field of view that often does not cover the same area of interest. Then two images are mapped in their field-of-view (domain Ω) to intensity values

$$A : x_A \in \Omega_A \mapsto A(x_A) \tag{3.2}$$
$$B : x_B \in \Omega_B \mapsto B(x_B) \tag{3.3}$$

Sampling and resolution should be take into account in $\mathbf{T}$, where the floating image must be re-sampled on a original grid by determining the intensity of each original grid point. For iterative registration algorithms, interpolation is necessary at each iteration for any realistic transformation.

The registration process involves recovering the spatial transformation $\mathbf{T}$ so that both $A(x_A)$ and $B^{\mathbf{T}}(x_B)$ will represent the same location. We refer to $\Omega^{\mathbf{T}}_{A,B}$ as the overlapping portion of the domains Ω_A and Ω_B.

$$\Omega^{\mathbf{T}}_{A,B} = \left\{ x_A \in \Omega_A | \mathbf{T}^{-1}(x_A) \in \Omega_B \right\} \tag{3.4}$$

A large variety of similarity measures has been proposed. They can be divided according to the type of information used to construct them. Registration algorithms that use geometrical features determine the transformation $\mathbf{T}$ taking into account sets of image points x_A and x_B that correspond to the same feature in both images.

Spatial correspondence may not exist when:

- Features change between source and target image acquisition. For example, tumor growth or organ contents change.
- One (or both) images are corrupted. For example, motion artifacts.
- Specific structures present in one image are not present in another. Because of this, the need of external markers in PET and MR modalities arises.

3.2 Rigid Transformation

Assuming that the imaged structure does not change shape or size between the different images, as in our case, one can use a rigid transformation. This has six degrees of freedom, three rotations about each of Cartesian axes and three translations along them.

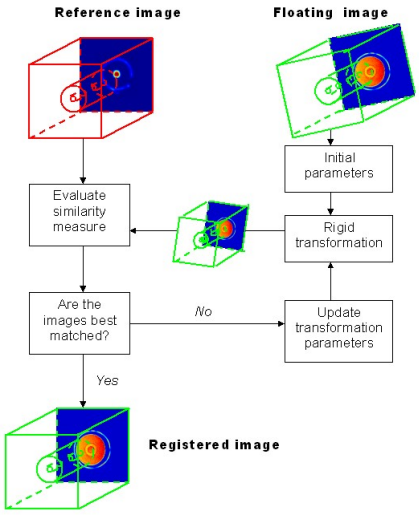

Figure 3.1: Flow-chart of the general algorithm to register images. The algorithm updates iteratively and new parameter values are tried until the maximum similarity (or minimum error) is found

The important consequence is that all distances are preserved. *A rigid transformation preserves angles as well as distances.* A good reference for projective geometry is [18].

Points in $\mathbf{R}^3$ are represented as a homogeneous vector in $\mathbf{R}^4$. Given an $h \in \mathbf{R}$ ($h \neq 0$), the point $(x, y, z)^T \in \mathbf{R}^3$ in world coordinates, is represented as $(h_x, h_y, h_z, h)^T \in \mathbf{R}^4$ in homogeneous coordinates. As an opposite manner, a point $(x', y', z', h')^T \in \mathbf{R}^4$ in the homogeneous coordinate system corresponds to the point $\left(\frac{x'}{h'}, \frac{y'}{h'}, \frac{z'}{h'}\right)^T \in \mathbf{R}^3$ in the world coordinate system. To translate a distance t_x in the x-direction, t_y in the y-direction, and t_z in the z-direction a transformation $x' = T(t_x, t_y, t_z)x$ is required.

$$T(t_x, t_y, t_z) = \begin{pmatrix} 1 & 0 & 0 & t_x \\ 0 & 1 & 0 & t_y \\ 0 & 0 & 1 & t_z \\ 0 & 0 & 0 & 1 \end{pmatrix} \tag{3.5}$$

Rotations are defined with respect to each axis.

$$R_x(\phi) = \begin{pmatrix} 1 & 0 & 0 & 0 \\ 0 & \cos\phi & -\sin\phi & 0 \\ 0 & \sin\phi & \cos\phi & 0 \\ 0 & 0 & 0 & 1 \end{pmatrix} \tag{3.6}$$

$$R_y(\theta) = \begin{pmatrix} \cos\theta & 0 & \sin\theta & 0 \\ 0 & 1 & 0 & 0 \\ -\sin\theta & 0 & \cos\theta & 0 \\ 0 & 0 & 0 & 1 \end{pmatrix} \tag{3.7}$$

$$R_z(\psi) = \begin{pmatrix} \cos\psi & -\sin\psi & 0 & 0 \\ \sin\psi & \cos\psi & 0 & 0 \\ 0 & 0 & 1 & 0 \\ 0 & 0 & 0 & 1 \end{pmatrix} \tag{3.8}$$

$$R(\phi, \theta, \psi) = R_z * R_y * R_z = \cdots \tag{3.9}$$

$$\cdots = \begin{pmatrix} \cos\theta\cos\psi & (\sin\psi\sin\theta\cos\psi - \cos\phi\sin\psi) & (\cos\psi\sin\theta\cos\psi + \sin\phi\sin\psi) & 0 \\ \cos\theta\sin\psi & (\sin\psi\sin\theta\sin\psi + \cos\phi\cos\psi) & (\cos\psi\sin\theta\sin\psi - \sin\phi\cos\psi) & 0 \\ -\sin\theta & \sin\phi\cos\theta & \cos\phi\cos\theta & 0 \\ 0 & 0 & 0 & 1 \end{pmatrix}$$

The complete transformation for the six parameters $[\phi, \theta, \psi, t_x, t_y, t_z]$ of a point $\mathbf{x} = (x, y, z, h)$ in homogeneous coordinates can be represented after transformation

$$\begin{pmatrix} x' \\ y' \\ z' \\ 1 \end{pmatrix} = \begin{pmatrix} R_{11} & R_{12} & R_{13} & T_{14} \\ R_{21} & R_{22} & R_{23} & T_{24} \\ R_{31} & R_{32} & R_{33} & T_{34} \\ 0 & 0 & 0 & 1 \end{pmatrix} \begin{pmatrix} x \\ y \\ z \\ 1 \end{pmatrix} \tag{3.10}$$

Representation in quaternions and some singularities of the parametrization in homogeneous coordinates are shown in [19].

3.3 Interpolation Methods

Resampling is required for each transformation in the registration optimization process. A great variety of methods were used with different names in image processing in accordance with Shannon's information theory [20]. It became relevant in medical image processing [21, 22, 23] which are summarized here. The computational cost of interpolation is normally too high to be used in each iteration, so lower-cost interpolation techniques must be used. Various techniques can be applied. One uses lower-cost interpolation at the beginning, such as nearest neighbor or trilinear, and the final iterations apply a more expensive interpolation. Interpolated images are blurred due to the response frequency of interpolation methods that corresponds to a low-pass filter. Therefore registration errors caused by interpolation can be greater than the loss of precision resulting from blurring.

For image resampling the interpolation step reconstruct a three-dimensional continuous signal $s(x, y, z)$ from its discrete samples $s(k, l, m)$ with s,x,y,$z \in R$ and k,l,$m \in N^0$. The amplitude at the position (x, y, z) is estimated from its discrete neighbors. The convolution of the discrete volume samples with the continuous 3-D impulse response function ${}_{3D}h(x, y, z)$ of a 3-D reconstruction filter can be written as

$$s(x, y, z) = \sum_k \sum_l \sum_m s(k, l, m) \cdot_{3D} h(x - k, y - l, z - m) \tag{3.11}$$

The kernels are usually expressed as separable as possible, to reduce the computational complexity

$${}_{3D}h(x, y, z) = h(x) \cdot h(y) \cdot h(z) \tag{3.12}$$

The general piecewise nth-order polynomial kernel is

$$h(x) = \begin{cases} a_{0j} + a_{1j}|x| + \cdots + a_{nj}|x|^n, & \text{if } j \le |x| < j + 1 \\ 0, & \text{if } m \le |x| \end{cases} \tag{3.13}$$

where n is the order of the polynomials, $j = 0, 1, \cdots, m - 1$ determines the extent of the kernel, and $n = 2m-1$. Therefore, $(n+1)m$ coefficients a_{ij} can be solved by imposing constraints on the polynomials.

The ideal interpolation function (sinc function) is spatially unlimited, therefore three interpolation methods of finite kernel size are discussed here.

3.3.1 Nearest Neighbor

It simplifies the sinc function with a limited spatial kernel. The value $s(x)$ at the location x is chosen at the next known value $s(k)$. Only $N = 1$ point is required, then the convolution kernel is

$$h_0(x) = \begin{cases} 1, & 0 \le |x| < 0.5 \\ 0, & \text{elsewhere} \end{cases} \tag{3.14}$$

The Fourier transform of the nearest neighbor kernel shows a DC-constant interpolator. The sidelobes introduce strong aliasing and blurring effects, that are associated with

this kind of interpolation. Generally it is insensitive to translations up to 1 voxel. The sidelobe suppressions (SLS) is $> 6.77\ dB$. Only the value of the nearest voxel is assigned. Therefore, it is the most efficient interpolation method from the computation time point of view, but it shows a poor quality.

3.3.2 Linear Interpolation

The values of nearest neighbors are weighted by their distance to the point of interpolation. The linear approximation of the sinc function represents a triangular function

$$h_1(x) = \begin{cases} 1 - |x|, & 0 \leq |x| < 0.5 \\ 0, & \text{elsewhere} \end{cases} \tag{3.15}$$

This kernel corresponds to a low-pass filter, with the characteristic that the sidelobes are below 10%. The disadvantages are that the high-frequency components are attenuated. The SLS is $> 13.34\ dB$.

3.3.3 B-Splines (Cubic)

Splines are based on pieces connected. B-spline of degree n is defined as $\beta^n(x)$

$$\beta^n(x) = \underbrace{\beta^0 * \beta^0 \ \cdots \beta^0(x)}_{(n+1)times} \cdot \cdots \cdots = \sum_{k=0}^{n+1} \frac{(-1)^k (n+1)}{(n+1-k)!k!} (\frac{n+1}{2} + x - k)_+^n \tag{3.16}$$

where $(x)_+^n = (max(0, x))^n$ with $n > 0$, and

$$\beta^0(x) = \begin{cases} 1, & |x| < 0.5 \\ 0.5, & |x| = 0.5 \\ 0, & |x| > 0.5 \end{cases} \tag{3.17}$$

With $n = 3$ the cubic B-spline shows the best performance and computation time

$$\beta^3(x) = \begin{cases} \frac{2}{3} - \frac{1}{2}|x|^2(2 - |x|), & 0 \leq |x| < 1 \\ \frac{1}{6}(2 - |x|)^3 & 1 \leq |x| < 2 \\ 0, & elsewhere \end{cases} \tag{3.18}$$

This equation could be write also as

$$\beta^3(x) = h_3(x) = h_0 * h_0 * h_0 * h_0 \tag{3.19}$$

where h_0 is the nearest neighbor interpolation method.

The cubic B-spline function provides a favorable stopband response and the amplitude of the sidelobes is lower than 1%. Increasing the order of the spline improves the quality but also increases the smoothing effects. The SLS is approximately ∞.

The interpolation methods and their frequency responses are shown in figure 3.2.

3.4 2D Orthogonal Projections

To register the volume the similarity measure is based on external markers attached to the phantom (see section 6.2). Therefore, at each iteration three projected images with maximum intensity projection (MIP) are acquired from the floating volume. The orthogonal projections acquired with MIPs should contain the particular shapes determined by the external markers. Then these MIPs are segmented as binary images, and compared with the distance map obtained from the same segmented projections of the reference volume. A flow chart of the registration algorithm is shown in figure 3.3. This section explains all the theoretical issues related to the steps to achieve this feature based registration.

3.4.1 Maximum Intensity Projection

This visualization technique is usually used to visualize selectively the vascular data of interest due to its simplicity and efficiency. *MIP* allow us to visualize the maximum intensity voxel value along a given path in a $3D$ volume. Here, the three orthogonal planes determined are used as the projection surfaces, then for each row or column, only the maximum intensity voxel value is assigned to the pixel value in that projection. Therefore, for $3D$ data three orthogonal $2D$ projections are obtained (see figure 3.4). Many applications of *MIP* for visualization, registration and segmentation purposes are described in [24, 25, 26], respectively.

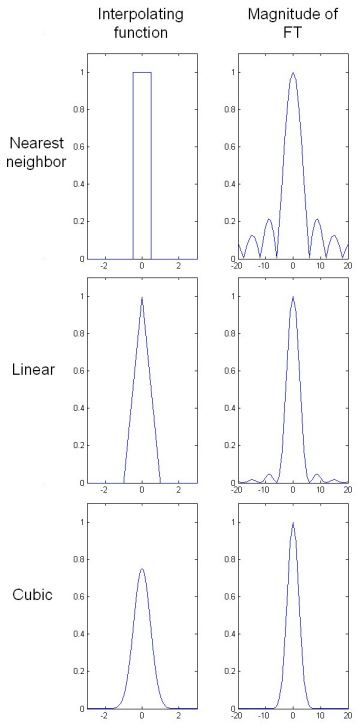

Figure 3.2: Interpolation functions and their FT

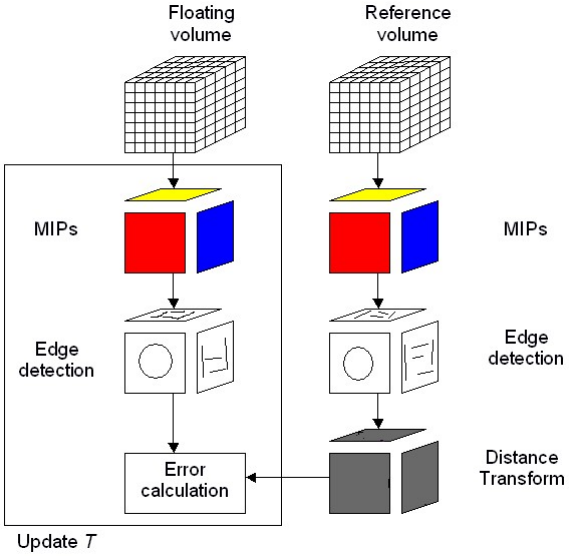

Figure 3.3: Flow chart of 2D orthogonal projections registration algorithm

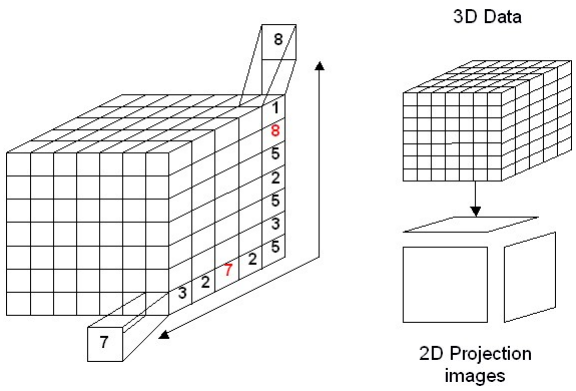

Figure 3.4: Scheme of the maximum voxel values extraction by MIP (Left). 2D orthogonal projections of a volume (Right)

3.4.2 Edge Detection

Edges occur where the intensity values in adjacent pixels have a large variation. They can be defined as step discontinuities in an image signal. There is a profuse literature about edge detection [27, 28, 29], that has its origin in the biological and computational communities. Edge detection is implemented by convolving with a specific linear filter, that usually approximates a first or second derivative operator. The peaks after taking the first derivative correspond to edges (intensity discontinuities) in an image. They correspond to zero-crossing values after applying the second derivative operator. Maxima in the output of the second derivative will correspond to tangent discontinuities (bars or lines).

Canny edge detection

The canny edge detector is actually widely accepted as a standard detector. J.F. Canny treated edge detection as a signal processing problem and the results of his Masther's Thesis was a design of an optimal edge detector. The main steps to achieve this simplest form of edge detection are the following:

1. Convolve the image with a $2D$ Gaussian filter.
2. Differentiate the image in two orthogonal directions.
3. Calculate the gradient amplitude and direction.
4. Obtain maximum values. The non-maximal gradient values are set to zero taking into account the gradient direction.
5. Threshold edges to eliminate insignificant edges.

Since convolution and derivative properties are associative, first the convolution of the image $J(x, y)$ with the Gaussian function is performed, then a smoothing version $I(x, y)$ of the original image is obtained.

$$I(x, y) = G(x, y) * J(x, y) \tag{3.20}$$

To detect edges in a particular direction, a two-dimensional mask is created. Convolving this mask with a one-dimensional edge detector aligned perpendicular to the edge is required. The gradient (∇I) of the image function I in a first order differential method is

$$\nabla I = \left[\frac{\partial I}{\partial x}, \frac{\partial I}{\partial y}\right] \tag{3.21}$$

$$M = \sqrt{\left(\frac{\partial I}{\partial x}\right)^2 + \left(\frac{\partial I}{\partial y}\right)^2} \tag{3.22}$$

$$D = \tan^{-1}\left(\frac{\partial I}{\partial x} / \frac{\partial I}{\partial y}\right) \tag{3.23}$$

where (M) is the gradient magnitude and (D) is the direction (see equations 3.22 and 3.23). Then any pair of orthogonal directions can be used, though x and y directions are usually selected.

In Canny detection a 3×3 approximation of the convolution mask to detect vertical edges defined to $\partial I/\partial x$, is

$$\begin{bmatrix} -1 & 0 & 1 \\ -1 & 0 & 1 \\ -1 & 0 & 1 \end{bmatrix} \tag{3.24}$$

$$\begin{bmatrix} -1 & 0 & 1 \\ -2 & 0 & 2 \\ -1 & 0 & 1 \end{bmatrix} \tag{3.25}$$

where the mask 3.24 is for the Prewitt operator and the mask 3.25 is defined for the Sobel operator. The latter puts more emphasis to the centre cell. To detect horizontal components similar mask are constructed to $\partial I/\partial y$.

The image is convolved with four masks, calculating horizontal, vertical and diagonal gradients. The direction that gives the higher result is used to determine magnitude and direction of the gradient at each pixel. To achieve the threshold two different values are used according to *thresholding hysteresis*. The high values of the edge detector assume the presence of edges but, due to noise, the output along an edge contour will be above the threshold half the time, showing breaking contours (*streaking*). The problem is resolved by applying two thresholds, the lower threshold can be 0.4 times the higher threshold to avoid this false edges. After comparing the results obtained with the lower and high threshold an edge list with valid edge points is created.

Problems that affect edge detector performance are the choice of the threshold and the masks. For instance, by varying the image size, leaving the intensity values invariant, a new edge detection should be made due to the change of the gradients. Therefore, estimation of the optimal threshold is not easy. Other problems include corners detection and detection of particular geometric features, such as lines and circles.

Criteria to evaluate the edge detector performance are: the probability of false edges detection and missing edges, errors in estimating the edge angle, the distance error between the detected edge and the real edge, and the tolerance to detection of corners and distorted edges.

Hough Transform

The Hough Transform can be used to extract any shape in an image. It requires the parametric form of the shape that can isolate regular curves such as lines, circles, ellipses. As a function of the complexity of the shape, the computational time changes. Tolerance to gaps in feature boundary descriptions and noise, is the main advantage of this technique. Assuming data after Canny edge detection the idea is to recognise the points that form a straight line. These points are evaluated for several combination of parameters. The parameters that represent the shape are iteratively evaluated. Those that win a majority

of votes are declared adequate for fitting the shape. They contribute to a global consistent solution by describing the best line given by these points.

Consider a point (x_i, y_i) in an image. The parametric equation of a line is

$$x\cos\theta + y\sin\theta = r \tag{3.26}$$

where θ and r are the parameters in the parametric equation. θ is the angle determined by the normal from the origin to this line, and r is the distance between line to the origin measured along the normal. Dividing the parameter space into a number of discrete accumulator cells, the votes can be collected between $0 < \theta < 2\pi$. r is limited by the size of the image. The use of parametric equations avoids infinite parameter spaces. A finite accumulator array to represent the votes for the parameters is needed. Resulting peaks in the accumulator array represent strong evidence that a corresponding straight line exists in the image. Then the centroid in near peaks that cover more than one accumulator has to be used for the estimation of the parameters.

Expressing a curve to detect as a function

$$f(a_1, a_2, \ldots, a_n, x, y) = 0 \tag{3.27}$$

any kind of curve can be detected. In the specific case of a circle the parametric equations in polar coordinates are

$$x = a + r\cos\theta \tag{3.28}$$
$$y = b + r\sin\theta \tag{3.29}$$

The parameters of this model are two for the centre of the circle (a, b) and the radius r. In order to determine the parameter space, equations 3.28, 3.29 are simplified by eliminating the radius in

$$b = a\tan\theta - x\tan\theta + y \tag{3.30}$$

The Hough transform algorithm for circle detection is described as

1. Quantize the parameter space for a and b.
2. Set all the accumulator cells equal to zero.
3. Compute the gradient magnitude $G(x, y)$ and the angle θ at an edge point.
4. Increment all points in the accumulator array $M(a, b)$ along the line given by equation 3.30.
5. Centres of circles in image correspond to local maxima in the accumulator array.

In this case, the computational complexity of the algorithm begins to increase since the accumulator has three coordinates in the space. As a result, the computation time and the size of the accumulator increase polynomially with the number of parameters. Descriptions of Hough transform are shown in [30] for circles and [31] for a time constant algorithm for Radon and Hough transforms. The Radon transform is closely related to the Hough transform, and computes projections of an image along specified directions.

3.4.3 Distance Transform

The general idea of a distance transformation (DT) is to obtain the distance from a point to an object. In this case the points are pixels. The distance assigned to a given pixel p corresponds to the distance to the nearest pixel q belonging to the object. The DT is the operation that computes the distance map from a binary image that represents the boundaries of a particular shape. There are many metrics to define the distance, Euclidean is usual, but other implementations are also valid, such as city-block, chess-board or quasi-euclidean.

$$\text{Euclidean} \quad \sqrt{(x_1 - x_2)^2 + (y_1 - y_2)^2} \tag{3.31}$$

$$\text{City-block} \quad |x_1 - x_2| + |y_1 - y_2| \tag{3.32}$$

$$\text{Chess-board} \quad max(|x_1 - x_2|, |y_1 - y_2|) \tag{3.33}$$

$$\text{Quasi-euclidean} \quad \begin{cases} |x_1 - x_2| + \sqrt{2} * |y_1 - y_2|, & \text{if } |x_1 - x_2| > |y_1 - y_2| \\ (\sqrt{2} - 1) * |x_1 - x_2| + |y_1 - y_2| & \text{otherwise} \end{cases} \tag{3.34}$$

where (x_1, y_1) is the spatial localization of pixel p in the image and similarly (x_2, y_2) for pixel q. In figure 3.5 the distance transform is shown for a detected circle with different metrics, the green pixels are closer to the feature than the yellow pixels.

The DT provides smooth characteristics and wide minima for object distances, which allows the use of fast optimization algorithms to match patterns. It avoids narrow minima that other methods have, such as correlation or difference between images, that require the complete set of possible positions to be searched. Calculating the distances for all pixels could be problematic, from the point of view of computation time. Therefore, many techniques based on masks have been applied. Raster scanning requires at least a forward scan (from top-right to bottom-left) and a backward scan (from bottom-left to top-right) to give a chamfer distance that is only an approximation of the Euclidean distance. Therefore, producing distance transformations on digital images is not trivial. A profuse inspection of distance transformations is shown in [32].

3.5 Mutual Information (MI)

This method has been used in a wide manner for registration of 3-D multimodal medical images and is based on voxel similarity measures. The idea is to maximize the amount of shared information in two images, or, in other words, to reduce the amount of information in the combined image to avoid duplicate versions of similar structures. The measure of information in signal processing is Shannon-Wiener entropy H, developed for communication theory [33]. Mutual Information (MI) measures the statistical dependence between two random variables, or the amount of information that one variable contains about the other. Then the MI of the image intensity values is maximal when the images are geometrically aligned. Descriptions of MI applied to medical purposes are discussed in [34, 35, 36].

3.5.1 Information theory applied to images

If we consider two images A and B as discrete random variables, each of them has marginal probability distributions $p_A(a)$ and $p_B(b)$ and a corresponding joint probability distribution $p_{AB}(a, b)$. The maximum dependence occurs when $T : p_A(a) = p_B(T(a)) = p_{AB}(a, T(a))$. The available information in an image is measured by entropy H

$$H = -\sum_i p_i \log p_i \tag{3.35}$$

where $p_1, p_2, ..., p_n$ are the histogram entries for a given image. Then we have two values at each voxel location for an iteration in the process to find the transformation T. The amount of information of the two images combined is the joint entropy

$$H(A, B) = -\sum_a \sum_b p^T_{AB}(a, b) \log p^T_{AB}(a, b) \tag{3.36}$$

The joint probability distribution of two images is estimated by calculating a normalized joint histogram. The marginal distributions are obtained by summing over the rows, respect the columns, of the joint histogram. For all voxels ($x_A \in \Omega^T_{A,B}$) in the overlapping regions of the images the intensity is plotted against the intensity of the corresponding voxel in B^T. Normalizing by the total number of voxels N in $\Omega^T_{A,B}$, a probability density function is obtained (PDF). The number of elements in the PDF is determined by the range of partitioned intensity values in the two images. The use of 64 or 256 bins is common. The information contributed by the individual images is the entropy of the part of the image that overlaps with the other image volume:

$$H(A) = -\textstyle\sum_a p^T_A(a) \log p^T_A(a) \quad \forall A(x_A) = a | x_A \in \Omega^T_{A,B} \tag{3.37}$$

$$H(B) = -\textstyle\sum_b p^T_B(b) \log p^T_B(b) \quad \forall B^T(x_A) = b | x_B \in \Omega^T_{A,B} \tag{3.38}$$

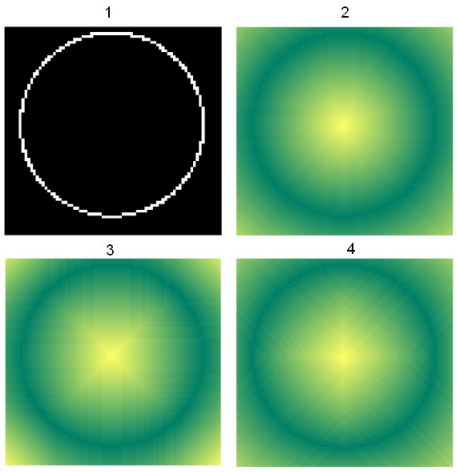

Figure 3.5: Distance transform. 1) Binary image with the shape of the circle. 2) Euclidean. 3) City-block. 4) Chess-board

3.5.2 Mutual Information

The mutual information taking into account the joint entropy is expressed in 3.39

$$I(A,B) = H(A) + H(B) - H(A,B) = \sum_a \sum_b p^T_{AB}(a,b) \log \frac{p^T_{AB}(a,b)}{p^T_A(a) \cdot p^T_B(b)} \tag{3.39}$$

$$= H(A) - H(A|B) \tag{3.40}$$

$$= H(B) - H(B|A) \tag{3.41}$$

where $H(A|B)$ represents the conditional entropy of image B given by image A, and similarly to $H(B|A)$

$$H(B|A) = -\sum_{a,b} p(a,b) \log p(b|a) \tag{3.42}$$

For $I(A,B)$ to be useful as registration criterion, this measure should vary smoothly with the transformation parameters T. This is certain for structures in different modalities, though the same structure or tissue corresponds to different intensity values. For example high-intensity values in the histogram of the CT correspond to bone, and bone correspond to low-intensity values in MR. When the bone structures are correctly aligned a peak is shown in the joint histogram. Although studies revealed the convergence of MI to the registration solution for a large range of translations and rotations, there are cases in which MI fails. These cases could be due to insufficient mutual information between the images, ambiguity about the intensity relationship, or a too small number of samples. The MI criterion assumes that the statistical relationship between images is identical over the area of overlap, so it requires a sufficient number of voxels. Therefore for low-resolution images or for a small area of overlap, the statistical relationship is not robust. This result in local optima shown around the correct registration solution.

To remove the MI dependence on overlap volume the combined information should be normalized. Two main normalization schemes have been proposed

$$ECC(A,B) = 2 \cdot \frac{I(A,B)}{H(A) + H(B)} \tag{3.43}$$

$$NMI(A,B) = \frac{H(A) + H(B)}{H(A,B)} \tag{3.44}$$

with $0 \leq ECC \leq 1$ and $1 \leq NMI \leq 2$. ECC is the entropy correlation coefficient and NMI is the normalized mutual information coefficient. The relation between both normalization schemes is

$$ECC = 2 \cdot \left(1 - \frac{1}{NMI}\right) \tag{3.45}$$

Preference for the NMI criterion due to superior maximization, in case of a small area of overlap, was found by Studholme et al. (1999). However, mutual information and normalized mutual information have been shown to perform equivalently in another study (Holden et al. 2000).

New adaptions of the MI measure to include spatial information have been developed recently. Several authors have introduced edgeness measures such as the gradient magnitude. Others considered the co-occurrence of neighboring voxel intensities and defined a second-order mutual information. These new approaches allow for the application of this technique to new registration methods.

It should be noted that the robustness of the MI registration algorithm depends on the interpolation method applied. Nearest neighbor and trilinear interpolation show local optima surrounding the best solution by introducing new intensity values which are not present in the reference image. New interpolation methods [35], such as the trilinear partial volume distribution method, give a smooth MI basin that attracts the optimization algorithm to the correct optimum.

It has been shown that MI is very robust to images affected by noise or intensity inhomogeneity and it was also applied successfully in multi-resolution optimization strategies.

3.6 Simplex optimization method

In this work six parameters should be taken into account simultaneously in order to optimize the solution. This parameters correspond to three translations and three rotations. Each of these is independent of the others. Therefore, a nonlinear multidimensional unconstrained optimization is required. The idea is to make in each iteration test points associated with their function values, and the iteration finalizes with new set levels. A description of the algorithm is found in [37].

Chapter 4

3D Segmentation

According to section 1.4, in this report 3D-region based segmentation methods are needed to obtain the MR based attenuation map. First the semi-automatic method seeded region growing and subsequently automatic region merging is explained.

4.1 Seeded Region Growing (SRG)

Region growing requires an initial location of seeds. Seeds are voxels that the operator identifies to correspond to specific tissues to be segmented. Once the algorithm starts, the seeds grow and finally different $3D$ regions are obtained. At each iteration the algorithm takes into account the intensity values in the surrounding voxels that participate in the growing procedure. If the criterion of homogeneity is satisfied, the voxel is classified into the same class as one or more of its neighbors. Various homogeneity criteria can be applied but, due to its simplicity, a threshold that evaluates the difference between the intensity voxels is applied. The algorithm stops when it detects that no more voxels can be treated and assigned to a region. Depending on the number and location of the seeds some voxels might remain unclassified. A good segmentation result depends on the correct positioning of the seeds, and this requires manual intervention. Problems related to the localization of the seeds in atypical voxels that are not representative of the region statistics should be avoided. Therefore, the knowledge of the operator can affect the segmentation results. Finally it should be said that this technique is not used for complex $3D$ volumes but it shows to be efficient to segment large and uniform regions. The method is explained in [38].

The algorithm starts with the localization of seed points that are grouped in n sets: $A_1, A_2, \ldots, A_n$. An individual set could consist of a single point. At each iteration of the algorithm one new voxel is assigned to one of the sets A_i, $i = 1, 2, .., n$. We call T to the set of unallocated voxels neighbors to one of the regions

$$T = \left\{ x \notin \bigcup_{i=1}^{n} A_i | N(x) \bigcap \left(\bigcup_{i=1}^{n} A_i \right) \neq 0 \right\} \tag{4.1}$$

where $N(x)$ is the set of immediate neighbors of the voxel x. In this case it is the 26-connectivity. Each step takes one voxel of T and labels it to one of the regions with

which $N(X)$ neighbors of the voxel intersect $(N(x) \cap \cup A_i)$. Now $N(x)$ is examined to calculate the distances from the neighboring regions

$$\delta(x) = \left[g(x) - \text{mean}_{y \in A_i(x)} | g(y)\right] \tag{4.2}$$

that represents the difference between the intensity in x and the mean intensity value of those regions. The voxel is assigned to the closest region taking into account the distance

$$\delta(x) = \min_{x \in T} \{\delta(x)\} \tag{4.3}$$

The elements of T are stored in a sequentially sorted list (SSL). It contains the coordinates of the voxels and the distance δ from the neighboring regions. The algorithm is as follows:

1. Initialization. Label the voxels according to their initial region.
2. Compute the neighbors T and introduce them in the SSL.
3. If the list is not empty, the first voxel y is removed from the SSL.
4. If all neighbors of y that have been labeled have the same label, then set y to this label.
5. Update the mean of the corresponding region.
6. Add neighbors of y which are not already labeled, or already on the SSL, to the SSL according to their δ values.
7. If step 4 is not true, then label y as boundary voxel.
8. Iterate the process by going back to step 3.

Problems involved in applying seeded region growing (SRG) to high textured images does not result in the desired segmentation because the algorithm stops before the best solution. The same problem is found in images with high intensity variation. The robustness in the presence of noise should be also tested for this segmentation technique. Although SRG algorithm is a semi-automatic method, it is possible to automate the process. An application of the SRG method to MR data is found in [39] and a unseeded $3D$ segmentation method is discussed in [40].

4.2 Region Merging (RM)

Region merging is region-based segmentation method that constructs homogeneous regions through the merging of voxels that have similar properties. One basic strategy is to compute the mean of the intensity values in the region, then the algorithm starts assigning the first region to the first voxel of the volume. Merging of the traversed voxels is decided if the intensity is close to the mean intensity of the region. If it occurs a new

mean intensity value is computed. If no merging with neighboring regions is possible, then it tries with non-neighboring regions. In the case that it is impossible to assign to any region, a new region is constructed. The merging algorithm stops when all the voxels have been treated. The basic rule to merge regions with a voxel x can be given as

$$\delta(x) = \Big[g(x) - \text{mean}_{y \in A(x)} | g(y)\Big] < \epsilon \tag{4.4}$$

where $\delta(x)$ represents the difference between the intensity in x and the intensity mean value of the region A, where ϵ is the threshold value. The algorithm is as follows

1. Initialization. Label the first voxel to the first region.
2. Select the next voxel y in a frames-rows-colums way.
3. Compute the four nearest intraframe neighbors and the nine nearest neighbors of the previous frame (T).
4. Compare the difference between the intensity value $g(y)$ and the mean intensity values of each of the regions assigned to T.
5. At least one region satisfies the step 4, taking account a given threshold. If there is more than one region, the region with the lowest intensity difference is chosen.
6. Merging is allowed, y is labeled.
7. If step 5 is not true, then try to merge y to any other possible region.
8. If step 7 is not true, then create a new region.
9. Update the mean of the corresponding region.
10. Iterate the process by going back to step 2.

Problems related with the statistics of the image are relevant in the segmented volume (of region merging). For example regions with low variance and close mean values are easily merged, because small regions have a large probability for merging than large regions. Another problem in the creation of false regions that correspond to the transitions between different objects. These should be treated as segmented boundaries instead of real whole regions. A study of an adaptative region merging technique is shown in [41].

Chapter 5

Attenuation Map

Quantitative images enable to translate voxel intensities into activity concentration. The image is degraded by several physical factors: the attenuation of the photons traveling towards the detectors, the imperfections in the detection of scattered photons, the finite spatial resolution of the imaging system, the limited number of counts that can be collected and the patient motion. The development of a reliable attenuation correction is one ingredient in the process of obtaining quantitative positron emission tomography images.

The problem of photon attenuation in emission tomography lies in the natural property that photons emitted by the radiopharmaceutical interact with tissues as they pass through the body. For typical photon energies in PET ($\approx 511\ keV$) the interaction of radiation with matter is described in section 2.3.2. Compton scattering forms the main source of attenuation ($> 99.7\%$ for water). The magnitude of photon attenuation is given in equation 2.9 and typical attenuation coefficients in table 2.1.

Typical reconstruction artifacts without attenuation correction show a depression of activity in the areas that are more in the center of the body. Because of the different thickness of tissues for each patient or animal the magnitude of photon attenuation varies locally in the body. Therefore, reconstruction of tomographic images without attenuation correction can cause errors in the amount of detected coincidences, resulting in reduced image contrast.

Current attenuation correction strategies in emission tomography have been developed [42, 16]. A transmission scan can be used to determine the attenuation correction before and after the PET tracer is administered. It measures the annihilation photons in coincidence as they pass through the body from an external source. However, the results are not acceptable enough for estimating tracer uptake in small tumors. The CT-based attenuation corrections require registration and segmentation. The linear attenuation coefficient measured at the x-ray energy is scaled to the energy of the photon emitted by the radiopharmaceutical in PET. The photoelectric effect and Compton scattering have different contributions depending on the photon energy in the tissues, because of that different scaling factors are used for the classes. In this project only segmented MR based is used. After registration (see chapter 3) of PET/MR data, segmentation is required to identify the different classes that contribute to the attenuation (see chapter 4). To every voxel in the segmented MR volume an attenuation coefficient is assigned. The coefficient correspond to the class that the voxel belongs to. An initial attenuation map in

MR dimensions and voxel size is required. After having this initial MR attenuation map, it should be interpolated to PET dimensions. This method is sufficiently general to be applied to any region of the body, but many sources of error should be take into account: errors in the acquisition process, registration accuracy and errors in MR segmentation. However, the improvement in SNR that segmentation provides compared to other attenuation correction processing methods, makes this technique useful for developing the attenuation map.

Chapter 6

Data Acquisition

In this chapter all the experiments carried out at the Nuklearmedizinische Klinik are discussed. During the experiments I am able to learn how the medical equipment works, and how the acquisitions are made for each technique. After the meetings made at the Klinikum all the issues to proceed with the equipment in an adequate way are clarified. Then various data sets from different clinical modalities are acquired to apply the different registration and segmentation algorithms, for that purpose the data sets should be used to detect some errors that could be committed in the acquisition of the two modalities (PET and MR). All the work is made with a mouse phantom and external markers. Since PET and MR provide complementary information, some identical information must be presented in the two modalities in order to perform registration. Therefore the external markers are tubes filled with a mix of water and $^{18}F\text{-}FDG$ that is visible in the two modalities. The correct disposition of external markers determines the registration process. A full description of the protocol to acquire PET/MR images is explained for the last acquisition performed with the A-PET *Mosaic* (see section 6.5). Posterior validation with real mice and rats must be evaluated.

6.1 Introduction

Two multi-modality series are acquired for MADPET-I and A-PET with MR. One intra-modality acquisition is made with MR: the MR image is registered with a simulated functional PET image using MR.

MADPET-I (Munich Avalanche Diodes PET) was developed in the Klinikum rechts der Isar for small animal imaging purposes. It is based in avalanche photo-diodes and used for oncology investigations, the scanner acquires $2D$ slices from a volume, therefore displacement of the volume is required. A clinical MR *Siemens Sonata Maestro Class* is available in the Klinikum rechts der Isar for the experimental use. The acceptable resolution and low radiation dose make it useful to obtain anatomical information, it operates with a 1.5 T magnetic field. The animal PET scanner *Mosaic* developed by *Phillips* obtains faster PET images with acceptable resolution, due to these new features it has replaced MADPET-I.

6.2 Phantom

With a phantom, most of the factors decisive for image quality can be evaluated to obtain a data set free of artifacts and distortions. In the case that involves this project the pre-processing methods are treated for small animal data. Because of that the desired phantom has the typical dimensions of a mouse. Taking into account that this phantom is rigid, problems related to the movement of real animals can be avoided to point out the details that are important for the registration and segmentation methods.

The length of the phantom is 7 *cm*, and the diameter 3 *cm*. More information about detailed dimensions can be seen in figure 6.1. In order to help the registration process markers are disposed with particular shapes on the phantom. Then a feature based registration can be achieved. The presence of this common information in PET and MR data helps also the mutual information registration method. Several configurations of markers are proposed to achieve the best registration, they are explained in the following sections according to the modality involved in the process.

6.2.1 Experiments with the MADPET and the MR

Two experiments are made with MADPET-I (see figure 6.2) and MR (see figure 6.3). In the first experiment external markers are disposed along the phantom. This disposition is shown in the scheme (see figure 6.4). Many problems come up from this configuration: inadequate shape of markers, not enough slices from MADPET-I and noise and distortion presented in MR images. These problems force us to resolve the MR problems related to noise and distortion, subsequently a new MADPET-I/MR acquisition is made. The new disposition of markers is shown in the following scheme (see figure 6.5). This disposition is based on two rings around the phantom and a line along the side of the phantom. It determines an Euclidean coordinate system avoiding ambiguity in registration and showing the particular shapes for each projection. The main aim of this particular shapes is to be helpful in the registration process because they are presented in PET as well as in MR. The linear marker has a length according to the maximum displacement of MADPET's bed. Finally the two data sets were not good enough to perform a correct registration, the lack of common information in the data that come from the different modalities inhibit registration. Therefore, the PET/MR data sets obtained can not give the desired attenuation correction.

6.2.2 Experiments with the MR

Since problems are found for the registration of MADPET data, one successful experiment is carried out only with MR. The main aim of this intra-modality acquisition is to obtain a data set with a simulated functional PET image. For the simulated PET image with MR, the small receptacle of the phantom and the external markers are filled with water. For the normal MR acquisition the big receptacle is now filled with water. Then these data set are registered. The disposition of external markers is very similar to the last acquisition of PET/MR (see figure 6.6), with this measured data set registration and segmentation algorithms were carried out (see chapter 7 for the results). Finally, an approximation to

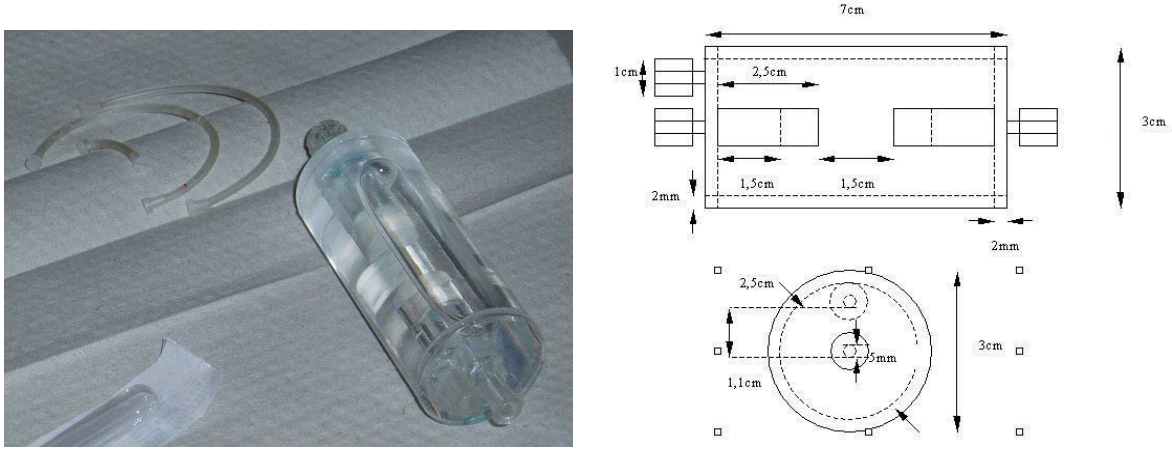

(a) Phantom and markers (b) Phantom dimensions

Figure 6.1: Small animal phantom

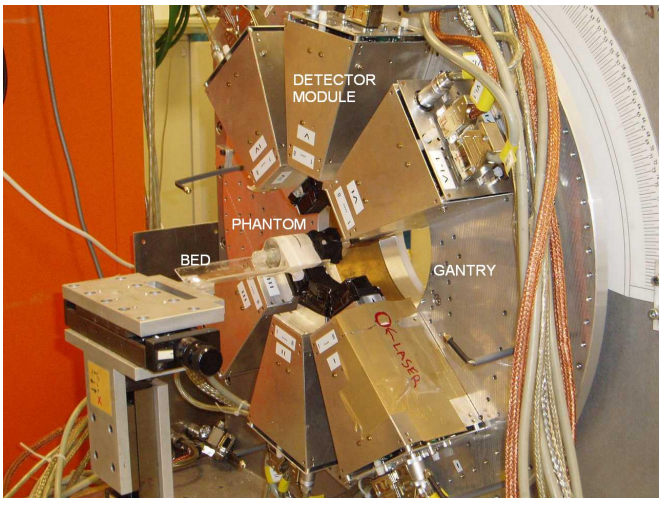

Figure 6.2: MADPET-I view

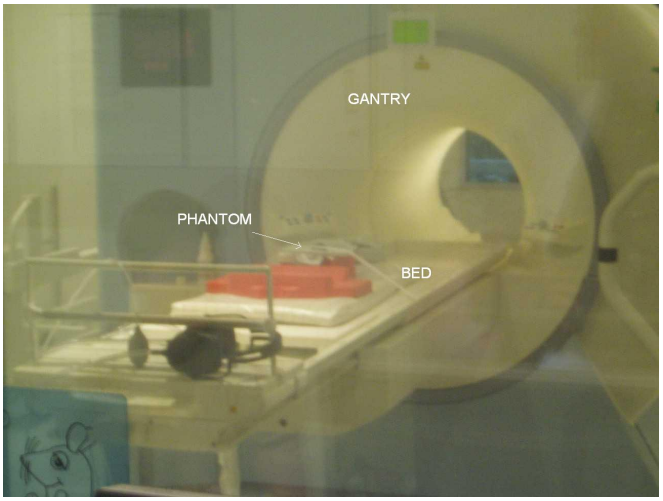

Figure 6.3: MR *Clinical Siemens Sonata Maestro Class* view

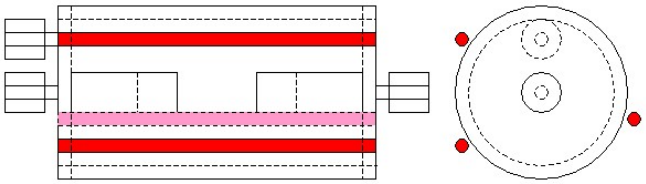

Figure 6.4: Disposition of external markers in MADPET/MR (Exp. #1)

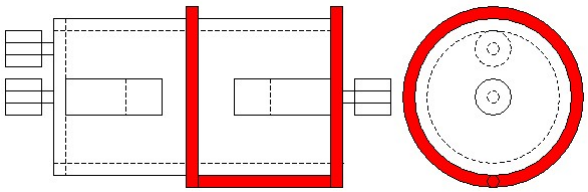

Figure 6.5: Disposition of external markers in MADPET/MR (Exp. #2)

obtain the attenuation map for the simulated PET data is provided.

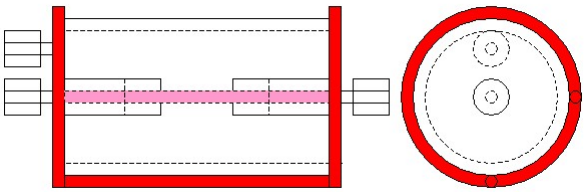

Figure 6.6: Disposition of external markers in the MR/MR Experiment

6.2.3 Experiments with the A-PET and the MR

A new animal PET scanner (*Mosaic*) developed by Phillips is acquired at the end of my stay. It shows significant advantages over MADPET-I. Preliminary results obtained with this system are discussed in this report. However, two acquisitions using A-PET and MR are made with the phantom, the disposition of the external markers in the first experiment is similar to the MR/MR case (see figure 6.6), but artifact problems affected the MR image. The second experiment forced us to decide a definitive best disposition of external markers that avoids artifacts in MR acquisition and maintains the Euclidean coordinate system (see figure 6.7).

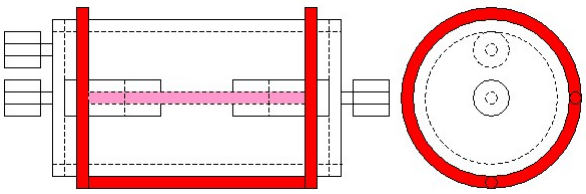

Figure 6.7: Disposition of external markers in the last *Mosaic*/MR Experiment

6.3 MADPET

Experiments #1 and #2 do not provide finally a data set good enough to perform registration, in spite of this, some aspects are interesting to discuss. These aspects are related to: voxel size and dimensions for each technique, attenuation compensation for each slice in PET, and noise in the MR images. From now only these relevant aspects are explained for Experiment #1, the results for Experiment #2 are shortly commented at the finish of the section.

Although the data obtained from the experimental MADPET-I are not stored in the DICOM standard, the storage parameters are known. The phantom is translated over 2 mm between two measurements, and the binary measurement data consist of a floating

point 128×128 pixels vector, with a pixel size of 1 mm^2. In Experiment #1, images are also acquired with clinical MR and CT. The parameters for CT and MR are extracted from the headers that are provided by the DICOM standard. Finally we can determine the voxel size and the dimensions for each data set (table 6.1) for the Experiment #1.

	Dimensions	Voxel size (mm^3)
PET	$128 \times 128 \times 4$	$1 \times 1 \times 2$
CT	$512 \times 512 \times 22$	$1.36719 \times 1.36719 \times 7$
MR	$512 \times 408 \times 23$	$0.138672 \times 0.138672 \times 1$

Table 6.1: Dimensions and voxel size for PET, CT and MR (Exp. #1)

Calculations about the radioactive decay should be made for each PET slice (see section 2.3.1 and equations 2.4 and 2.5). Then the decay factor for each slice is calculated knowing the acquisition time between PET slices (see table 6.2).

Slice	Decay factor
1	1
2	1.157
3	1.328
4	1.521

Table 6.2: Compensation factors for the activity decay in PET (Exp. #1)

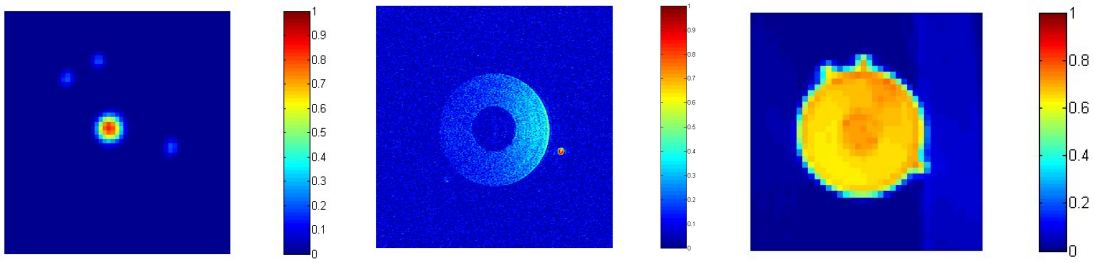

(a) PET (b) MR (c) CT

Figure 6.8: Acquisitions in the three modalities for the Exp. #1

As it can be seen in figure 6.8, the data is normalized between 0 and 1 as floating values. The slices shown are the 1^{st} slice from the PET acquisition, the 15^{th} slice from the MR acquisition, and the 16^{th} slice from the CT acquisition. MR and PET have very different spatial resolutions so a final decision should be made whether to choose the MR or PET image as target image in registration. The advantage of choosing MR is that spatial resolution is conserved in the final registered images.

Finally in the 3D volumes it can be seen that MR and CT well represents the shape of the phantom, though the PET volume only shows the functional information of the phantom (only four slices are acquired).

The initial disposition of markers is shown in figure 6.4. As can be seen in the MR image, only one marker is present in the reconstructed volume. This leads to the idea that the presence of noise corrupts the important data that is finally needed to make the registration of the volumes. Not all the markers are visible in the MR images due to noise problems, therefore only one of the three tubes in the MR images can be seen. More information from the PET data is required because the first acquisition has only four slices in order to do the registration. Finally, due to the sources of error commented before, the solution is not valid and this data set is not adequate.

It is needed the phantom to represent exactly an Euclidean coordinate system in both techniques, MR and PET, to avoid ambiguity in the position of markers. This fact affects registration. Besides, the MR image should be optimized in order to reduce the presence of noise. From now CT is discarded because the clinical PET/CT scanner resolution is not good enough. For Experiment #2 the disposition of markers is shown in figure 6.5. An amount of seven useful slices are acquired for PET with the same pixel size and the distance between PET slices is different in order to cover the whole region on which the external markers were presented. Subsequently, a MR acquisition is made with new dimensions and voxel size (see table 6.3). The decay factors are calculated for each slice in the same manner as for Experiment #1 (see table 6.4).

	Dimensions	Voxel size (mm^3)
PET	$128 \times 128 \times 7$	$1 \times 1 \times ?$
MR	$320 \times 320 \times 34$	$0.40625 \times 0.40625 \times 1$

Table 6.3: Dimensions and voxel size for PET and MR (Exp. #2)

Finally two main factors make the data set obtained in the Experiment #2 not useful, the different distances between slices in PET is a problem for registration. Because of that a pre-processing step is required: an initial interpolation to have the same PET/MR

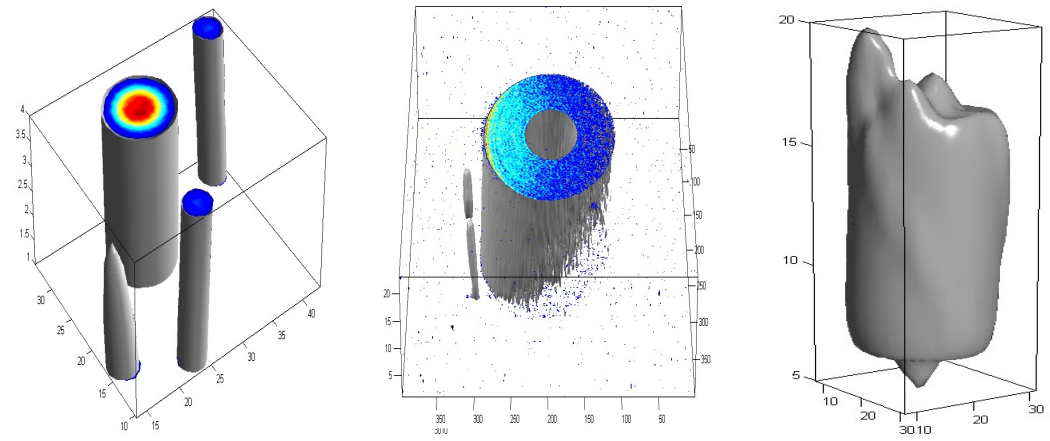

(a) PET (b) MR (c) CT

Figure 6.9: Reconstructed volumes for the three modalities for the Exp. #1

dimensions and voxel size for the axial direction is required. This operation introduces too much information that was not present at the beginning. The other problem is that the MR images are distorted. The distortion problem is discussed in the following MR section. Finally time is mainly invested in MR due to the arrival of the new animal PET scanner (*Phillips Mosaic*), as a consequence MADPET-I is definitively discarded.

6.4 MR

Previous MR acquisitions are commented in the section before. The distortion problem is the main problem found, but other problems that hampered subsequent registration and segmentation must be discussed. PET is the first technique to be acquired, and subsequently MR images are obtained. From one acquisition to another the phantom should be treated carefully: problems with the presence of air bubbles in external markers are not desirable in registration and segmentation processes, and the presence of asymmetric noise distribution affects the MR intensity values. Therefore segmentation can be seriously affected due to the value selection of the intensity threshold. If the noise level is too high this interferes with the thresholding needed for the segmentation process. The noise problem is easily resolved with an adequate MR *loop coil* configuration, because of that in the reconstructed volume the external markers are appreciated free of noise(see figure 6.10).

In order to get the best performance, two different data sets are taken. Every one has a distance between slices of 2 *mm* and one of them has an offset of 1 *mm* in the axial direction. The final volume is acquired from these, interleaving the two data sets. If we reduce the distance between slices in one data set, effects related to the reconstruction algorithm introduce spatial distortion in the image. Because of that the final volume comes from the two interleaved data sets (see figure 6.11).

The problem of the geometric distortion observed in MR affects registration. The phantom is displaced with respect to the external circular markers. In Experiment #2 can be observed that PET is unaffected by this distortion (see figure 6.12). Therefore it is impossible to establish an exact spatial correspondence.

In order to be sure that the source of displacement comes from the original data obtained from the MR, the Hough transform for circles (section 3.4.2) is applied to a

Slice	Decay factor
1	1
2	1.167
3	1.444
4	1.755
5	2.047
6	2.507
7	2.990

Table 6.4: Compensation factors for the activity decay in PET (Exp. #2)

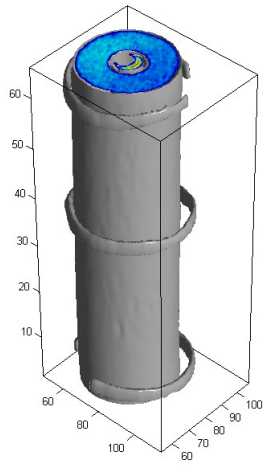

Figure 6.10: Reconstructed volume for MR in Experiment #2

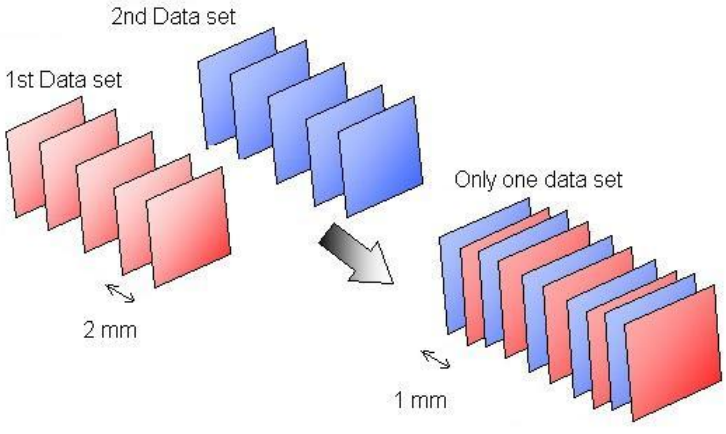

Figure 6.11: Interleaving of the two data sets acquired in MR

MIP view of the data (section 3.4.1). One circle is extracted from the shape of the external marker and another from the edge of phantom in the MR image. The distance between the circles is approximately of 3 pixels, then taking into account the voxel size this difference corresponds to 1.2 mm. This measure can be considered unacceptable prior to registration.

Various acquisitions changing the place (left, right, upper, lower) of the phantom are acquired for the MR scanner, the results indicate that the distortion is invariant with the position. A final acquisition with a small cylinder filled with fat and disposed along the side of the phantom revealed that the fat in this case is not affected by the distortion mechanism. Only the phantom is displaced with respect to the external circular markers.

Magnetic susceptibility is the ability of a substance to become magnetized. A possible explanation for the observed distortion is that the water in the tubes is magnetized to a different degree that the water in the phantom. The origin of this displacement is due to the different resonance frequency of the compound in the tubes and the water in the phantom. The compound is water mixed with $^{18}F\text{-}FDG$. This leads to a difference in precessional frequency and in phase of the magnetization vector in both compartments. The difference in precessional frequency is translated into a position shift in the image that contains the phantom with markers. For a given size of the field-of-view FOV (L) (i.e. 256×256 pixels) and a given receive bandwidth (BW) (i.e. $\pm 16kHz$), a frequency range of BW/L Hz per pixel is obtained. By increasing the BW or decreasing L increases the frequency range corresponding to our image pixel, resulting in a decrease in the position shift between the markers and the phantom. By increasing the receive bandwidth the displacement becomes less than 1 pixel. Because of that the dimensions of MR are changed. Each slice contains 256×256 pixels with a pixel size of 0.5 mm^2. Figure 6.12 shows the geometric distortion before and after changing the receive bandwidth.

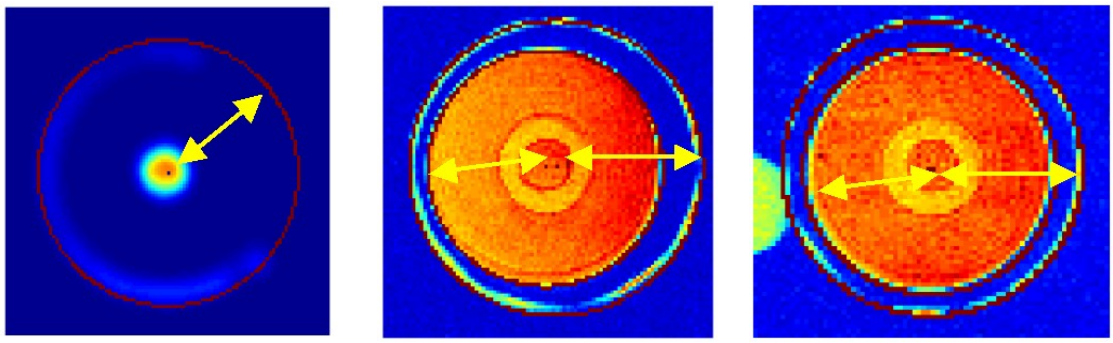

(a) PET without distortion (b) MR with distortion (c) MR without distortion

Figure 6.12: Geometric distortion obtained in MR acquisitions

After resolving the distortion problem the final MR dimensions and appropriate voxel size are selected. Then registration and segmentation of MR data are possible and finally an attenuation map correction can be determined. Subsequently to simulate the functional PET with a MR/MR acquisition the dimensions and voxel size are shown in table 6.5.

6.5 A-PET

Two experiments are made with the new scanner. The first disposition of the markers is shown in figure 6.6. While the PET acquisition is acceptable, the circular external markers are not presented due to artifacts in the MR acquisition. The system apparently can not handle large and sharp discontinuities in the spatial distribution of ^1H. When the markers are placed exactly at the borders of the phantom in the axial direction, the slices show a large number of circle segments. This distortion is absent when the markers are displaced slightly inwards along the axial dimension. Because of that a new configuration is suggested. Then the final disposition of markers is shown in figure 6.7. Finally a free artifact image is obtained from MR and therefore the attenuation correction is possible.

For this last acquisition the detailed protocol to acquire the PET/MR images is explained. First, filling and disposition of external markers is required, the tubes are *SURFLO ® Winged infusion set* and the tube characteristics are: 21 G $\times$ 3/4″, 0.8 $\times$ 19*mm UTW* and length 30 *cm*. The total volume admitted is 0.42 *ml*. Two circular tubes are required. For this purpose segments of the tube are needed. The length of the circular tubes is approximately 9.5 *cm*, the volume that can be introduced is 0.0875 *ml*. For the tubes that describe a line along the side of the phantom the length is approximately 4.5 *cm*, and the volume admitted is 0.0475 *ml*. The linear tubes are disposed 45° from each other along the side of the phantom.

The initial activity concentration is 344 μCi in 1 *ml* with a total activity volume of 2 *ml*. The external markers are filled with 0.25 *ml*. The small receptacle in the phantom is also filled with 0.25 *ml*. The final activity concentration introduced is 170 μCi in the total volume (small receptacle and external markers). Therefore the concentration is equally divided over the tubes and the small receptacle. After filling each external markers both ends of the tubes are closed with small screws and these markers are fixed to the phantom. The complete process takes approximately 30 minutes. The weight of the phantom with the external markers is 58.15 *g*, this measure is required by the A-PET software. The PET measurement time takes 6 minutes, and the reconstruction time 15 minutes.

After PET measurements the MR acquisition is required. The clinical MR *Siemens Sonata Maestro Class* scanner is disposed to accommodate the small animal phantom. It works with a 1.5 *T* magnetic field and a turbo spin-echo sequence (fast sequence). To work with a small animal phantom a small *loop coil* is used, the 18.5 *cm* of radius *loop coil* characteristics are 65 *MHz* and 1.5 *T*. Since the phantom contains a small amount of water, other receptacles with water are required to determine the resonance frequency (shimming). The MR images are *T*2 weighted. An initial faster acquisition is obtained to determine the region of interest, then two data sets with a distance between slices of 2 *mm*

	Dimensions	Voxel size (mm^3)
Simulated PET	$256 \times 256 \times 34$	$0.5 \times 0.5 \times 1$
MR	$256 \times 256 \times 34$	$0.5 \times 0.5 \times 1$

Table 6.5: Dimensions and voxel size for simulated PET and MR

are integrated in the same DICOM file. The MR acquisition process takes approximately 8 minutes for each data set. The final dimensions and voxel size for the A-PET/MR acquisition are shown in table 6.6.

	Dimensions	Voxel size (mm^3)
PET	$128 \times 128 \times 120$	$1 \times 1 \times 1$
MR	$256 \times 256 \times 34$	$0.5 \times 0.5 \times 1$

Table 6.6: Dimensions and voxel size for A-PET and MR

Chapter 7

Algorithm Results

The need for a data set good enough to test the registration and segmentation algorithms forced us to obtain a simulated functional PET image (see section 6.2.2).

For $2D$ orthogonal projections and Mutual Information registration methods the cost functions for rotations and translations are calculated. The influence of interpolation methods is also shown. Finally the different computation times for interpolation and registration methods are discussed. For seeded region growing and region merging segmentation methods differences taking into account valid results and computation time are shown.

Finally an approximation to the simulated PET attenuation map is obtained and various aspects are treated: effect of interpolation to PET image dimensions and non-assigned voxels in the segmentation process.

7.1 Display of Data

To test the validity of registration and segmentation methods only the region of interest to match is selected. This region comprises the pixel ranges $x = [83, 155], y = [90, 165]$ along the z-axis to minimize the computation time. The initial dimensions are shown in table 6.5. The disposition of external markers on the phantom (see section 6.2) is shown in figure 6.6, though is not the definitive scheme. The $3D$ visualization of the two data sets for a full and a multiple slice visualization are shown (see figures 7.1 and 7.2). Both contain the external markers (circles and lines). For the simulated PET image the slices represented are: $x = 41$, $y = 35$, $z = [9, 77]$, and for MR are: $x = 43$, $y = 37$, $z = [13, 81]$.

7.2 Registration Methods

As discussed in section 1.3 rigid transformation is selected (section 3.2). Two methods of similarity measure are developed: $2D$ orthogonal projections and MI (sections 3.4 and 3.5). The MR image is selected as reference image, and the optimization method used is simplex.

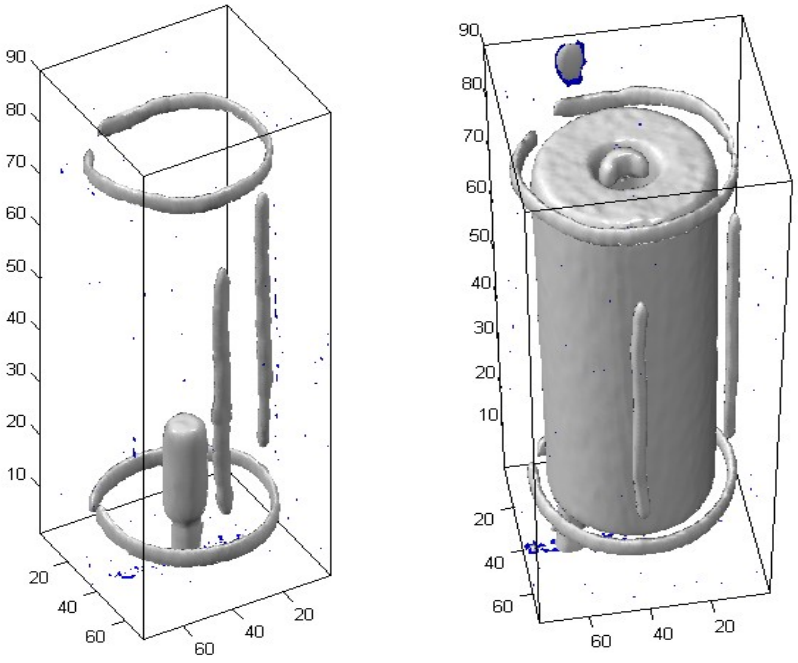

(a) Simulated functional PET (b) MR

Figure 7.1: Reconstructed volumes (MR/MR acquisition)

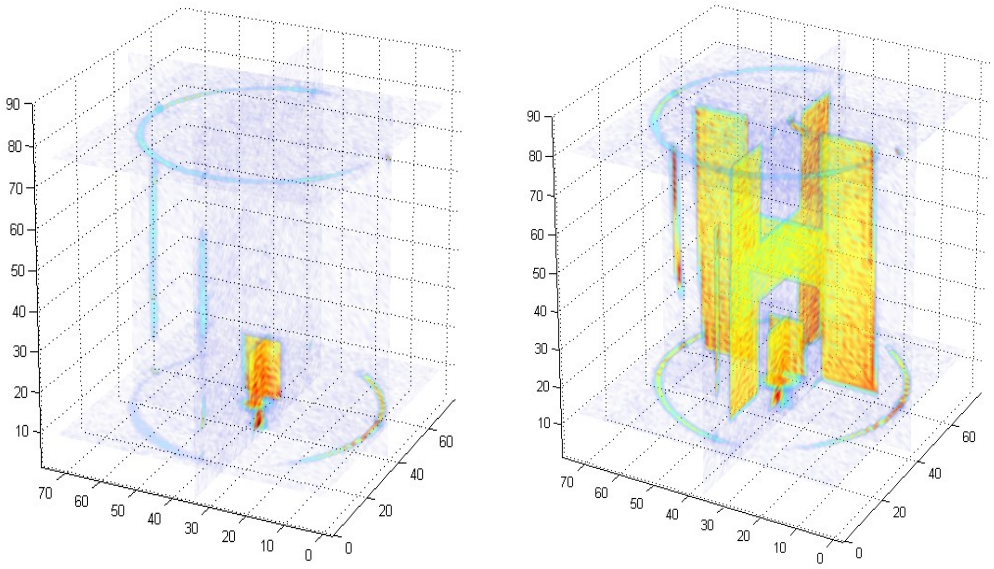

(a) Simulated functional PET (b) MR

Figure 7.2: Representative slices (MR/MR acquisition)

7.2.1 2D Orthogonal Projections

The algorithm consists of four main processes described in section 3.4. First, the MIPs criterion is selected. MIP shows the different shapes (circles and lines) to be identified in the two data sets (see figure 7.3). Various edge detectors (Sobel, Prewitt, Roberts, Laplacian and Canny) with different thresholds are tested for the different data sets acquired during the project. Only the Canny edge detector revealed to be a robust option. For the M projection the Hough transform to detect circles is maintained (see figure 7.4). In this project the Hough transform function can detect one or two circles, of a given radius in a single image. In the O projection the idea is to extract one of the linear markers by Canny detection. In the P projection the other linear marker is extracted. Many thresholds are applied to find the best Canny detection. Finally the change of intensity values in each iteration due to interpolation forces the threshold to be determined automatically by the MATLAB function *edge*.

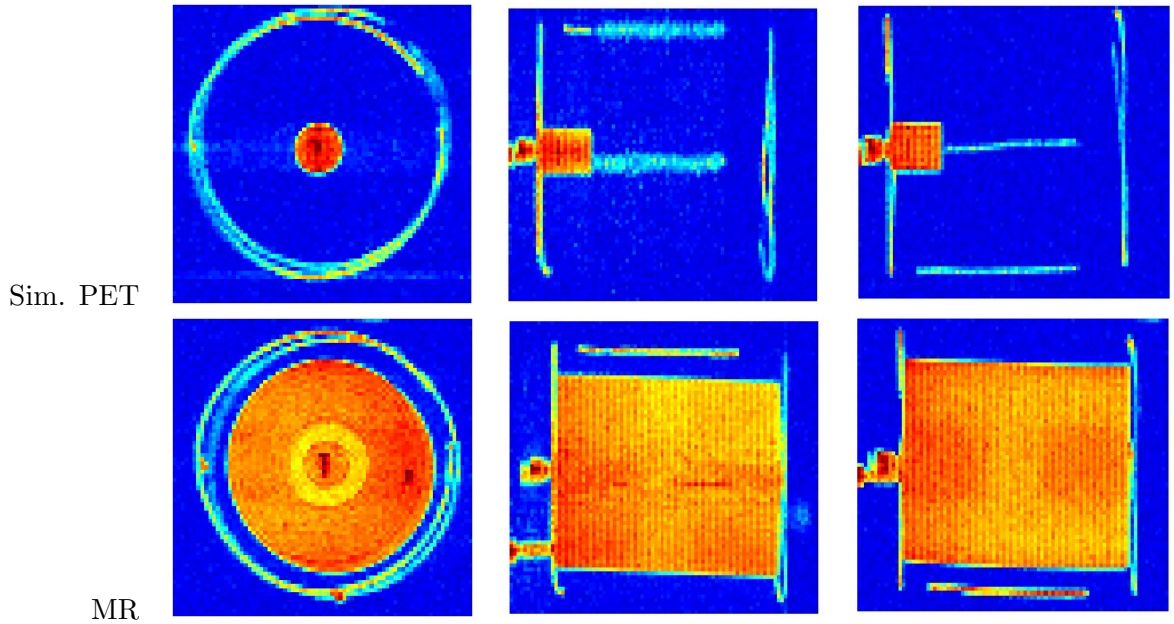

(a) M Projection (b) O Projection (c) P Projection

Figure 7.3: MIPs of the initial data sets

Edge detection (Canny and Hough transform) is applied to obtain finally the distance map for the reference volume projections. The metric selected is Euclidean in the MATLAB function *bwdist*. This process is computed only once before the optimization process is run (see figure 7.5).

A first estimation of the initial error is obtained (see figure 7.6). For this registration method the optimization process could not be performed with the simplex method. This is due to the high computation time needed with the implementation in MATLAB (MATLAB function *fminsearch*). Although a careful inspection of the cost functions is possible, it still gives an idea of the convergence of the algorithm.

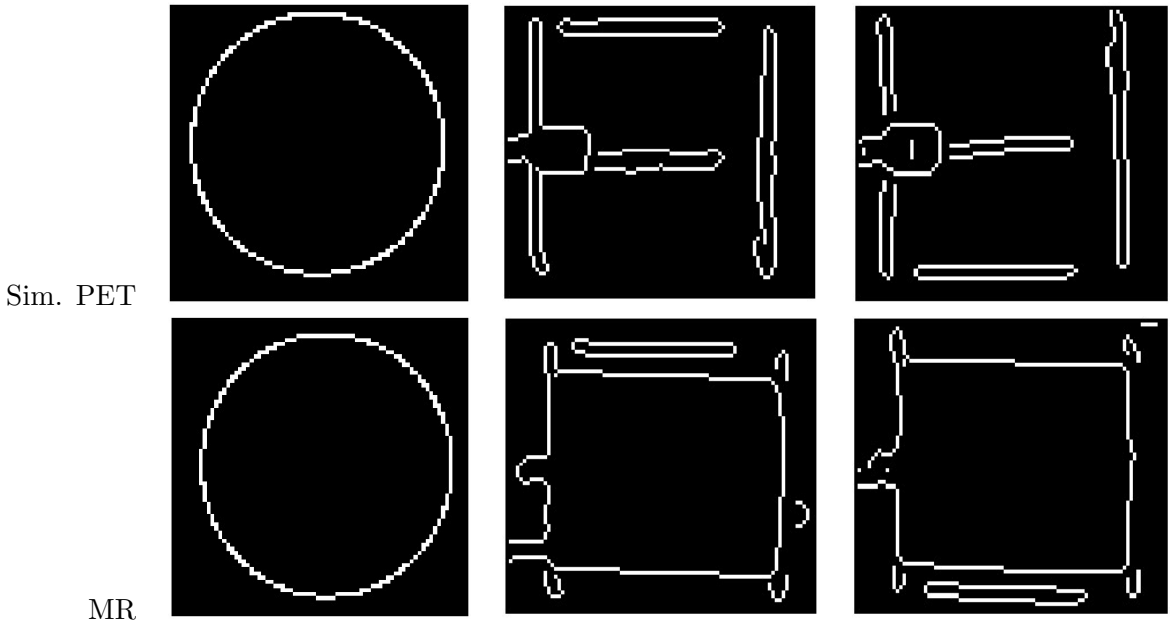

(a) M Projection (b) O Projection (c) P Projection

Figure 7.4: Edge detection of the initial data sets

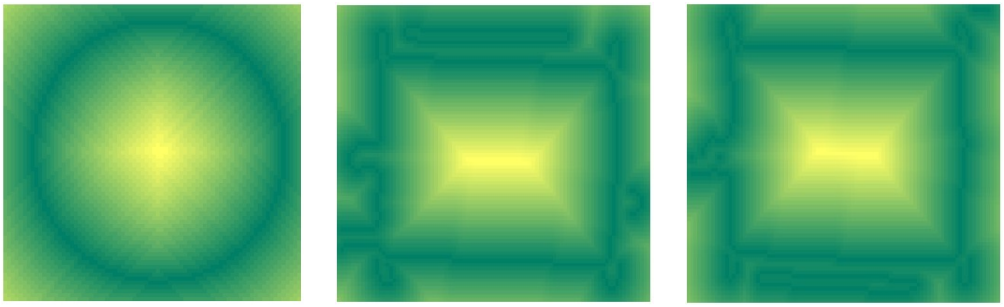

(a) M Projection (b) O Projection (c) P Projection

Figure 7.5: Distance map for the reference volume

Cost Functions

The cost functions are shown in detail in Appendix A.1. For the O and P projections the cost functions appear to be monotonous while for the M projections the cost functions show to be discrete. The Hough transform for some parameters of translation detects two circles instead one. Therefore, the binary image extracted contains more pixels assigned to features. Then the error is higher. Thus changes between iterations occur in a discrete manner that obstructs the optimization process. The effect of peaks is more abrupt for rotations than for translations. For Canny edge detection this does not occur because cost functions are smoothed. When the parameter space is sampled with a lower step, some local minima surrounding the solution can be visible. The needed to check the convergence of this algorithm require to test it in a faster implementation. Where the optimization algorithm can be tested for its applicability (e.g. C++).

7.2.2 Mutual Information

According to section 3.5 many steps are necessary in order to compute the Mutual Information registration between two volumes. To calculate the initial error the individual and joint histograms should be obtained (see figures 7.7 and 7.8). For the histograms the intensity values are mapped in a range from 0 to 256 bins. Subsequently the initial mutual information is computed (see figure 7.9).

Although all the functions required by MI are implemented in MATLAB, the speed requirements of the optimization algorithm made MATLAB not useful to find the registered solution. Therefore a registration software is used developed in the Chair for Computer Medical Aided Procedures. The registration solution is shown in table 7.1 for each parameter. The percentage of overlapping volume is approximately 90.91% in the final registration.

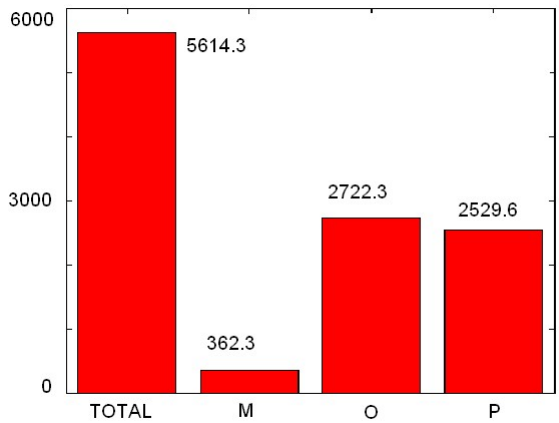

Figure 7.6: Initial error for 2D orthogonal projections

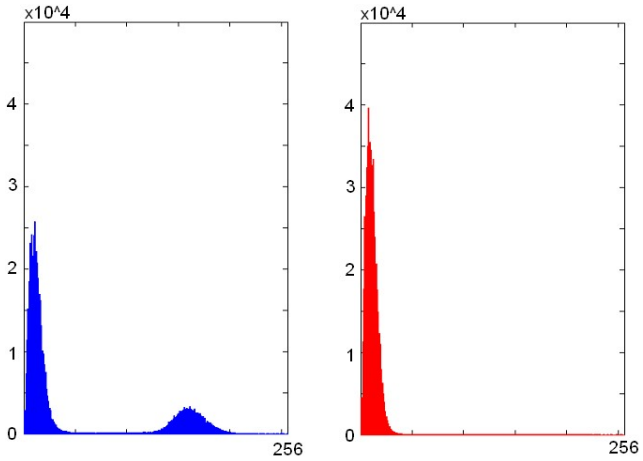

(a) MR histogram (b) PET histogram

Figure 7.7: Individual histograms for the non-registered data set (256 bins)

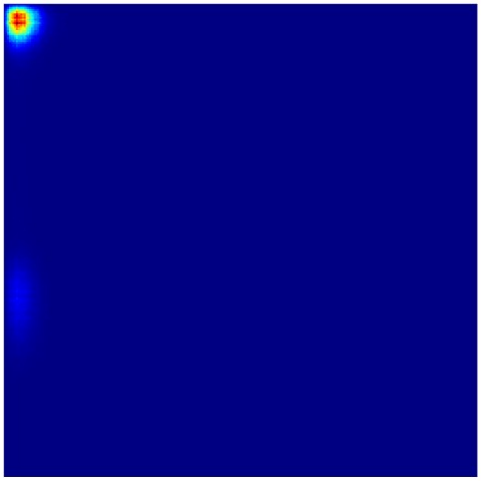

Figure 7.8: Joint histogram for the non-registered data set (256 bins)

	Parameter	Value
Rotations (rad)	ϕ	0.000266
	θ	0
	ψ	0.014078
Translations (mm)	t_x	-0.5
	t_y	-1
	t_z	-3.531250

Table 7.1: Registration parameters

Cost Functions

The cost functions are shown in detail in Appendix A.2. Normalized mutual information NMI is selected as registration criterion. MI shows a clear maximum in the registered position for a broad range of rotations and translations.

7.3 Registration Results

The final error and mutual information results are shown in table 7.2. The registered error for $2D$ ort. projections is near to 4600, which results in the conclusion that the error is less but not near to zero in the registration position. The MI value is 0.06. Taking into account the NMI value is 0.019, far away from 1, then not too much information between the volumes seems to be present. In spite of not having too much mutual information the registration is possible for the simulated PET/MR data sets with MI.

	$2D$ Ort. Projections	Mutual Information
Initial	5614.3	0.024757
Registered	4652.1	0.065451

Table 7.2: Initial and registered error and Mutual information for both registration methods

7.3.1 Interpolation Methods

The interpolation methods are explained in section 3.3. The cost functions for both registration methods are calculated for the three classes of interpolation: nearest, linear and cubic. The aim is to have an idea of the best interpolation method according to the cost function results (see figure 7.10) and the computation time (see figure 7.11).

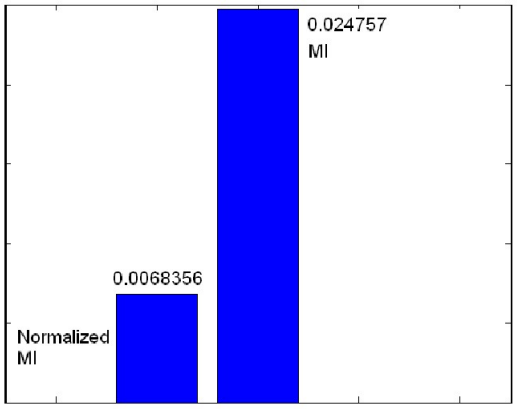

Figure 7.9: Initial Mutual Information and Normalized Mutual Information before registration

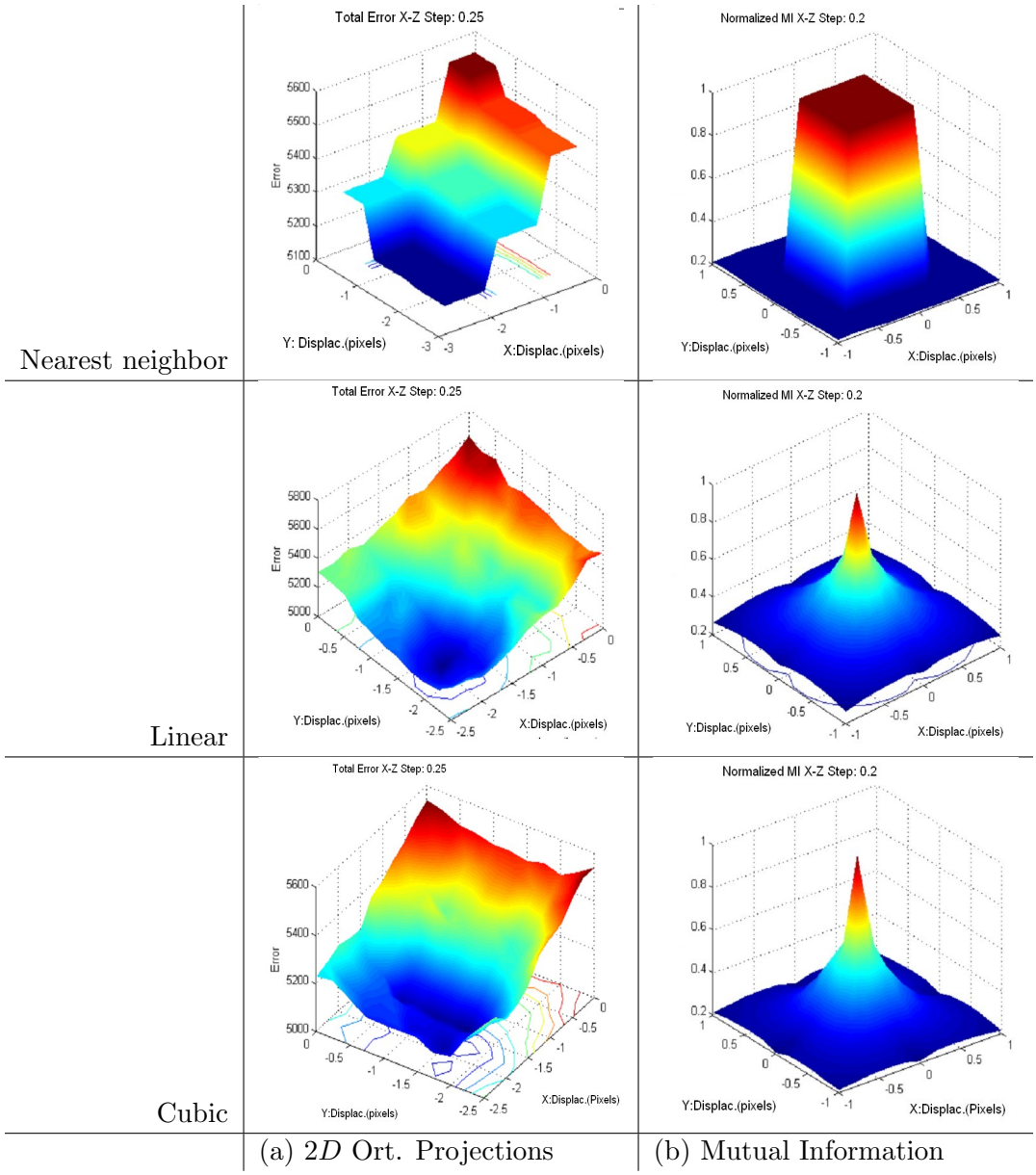

(a) 2*D* Ort. Projections (b) Mutual Information

Figure 7.10: Interpolation results for the cost function X-Z with a step of 0.2 pixels

The nearest neighbor interpolation method shows a stair effect for both registration methods. The difference between linear and cubic interpolation is that cubic interpolation shows more accurate cost functions. Taking into account the computation time in nearest and linear interpolation take approximately the same time and nearest interpolation is not a valid method for developing an accurate registration, then linear is better. Differences in MI for linear and cubic interpolation are clear. While linear interpolation shows a broad maximum, cubic interpolation shows a narrow maximum.

7.3.2 Multi-Resolution Techniques

Multi-resolution techniques have been applied successfully to MI. The aim is to test these techniques with the $2D$ orthogonal projections in order to know if they can be applied and, thus, reduce the computation time. The two data set dimensions are changed to $Z \times Z \times Z$, where Z acquires the following values: $10, 20, 30, 40, 50, 60, 70$. only for $Z = 20$ and $Z = 50$ values the visualizations of multi-resolution are made (see figure 7.12).

The cost function calculated for $20 \times 20 \times 20$, $2D$ ort. projection does not work because the features are not well extracted. The cost function show many peaks and local minima. In MI the cost function shows a clear maximum, though the cost function is curled in the region near to the solution. This can difficult the optimization task in MI. The cost function calculated for $50 \times 50 \times 50$, $2D$ ort. projections shows a minimum, but it presents the normal problems of this registration method. MI is less curled.

Figure 7.13 shows the different iteration computation times taking into account the volume dimensions. While $2D$ ort. projection computation times depend on the number of pixels presented in the orthogonal projections, MI computation times depend on the number of volume voxels. In other words, $2D$ ort. projection computation time is squares dependent on the high, length and width of the volume, while MI computation times maintain a cubic dependence.

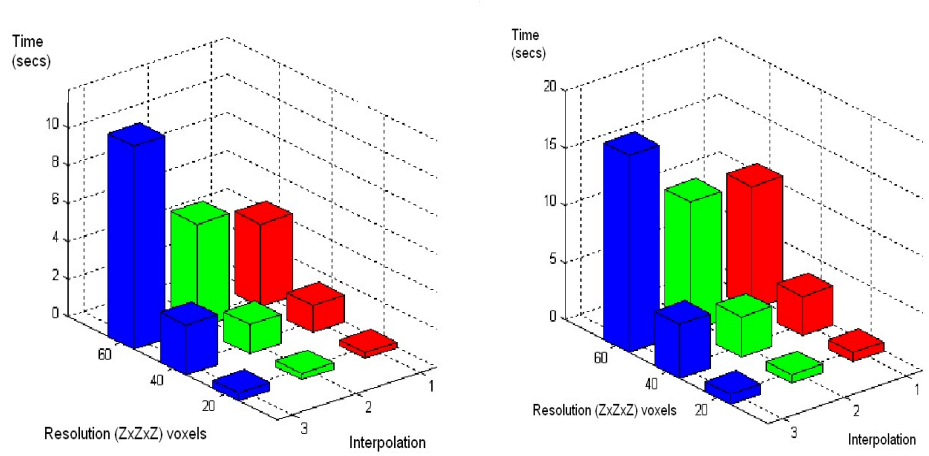

(a) $2D$ Ort. Projections (b) Mutual Information

Figure 7.11: Iteration computation time for each interpolation method: Cubic (Blue), Linear (Green), Nearest neighbor (Red)

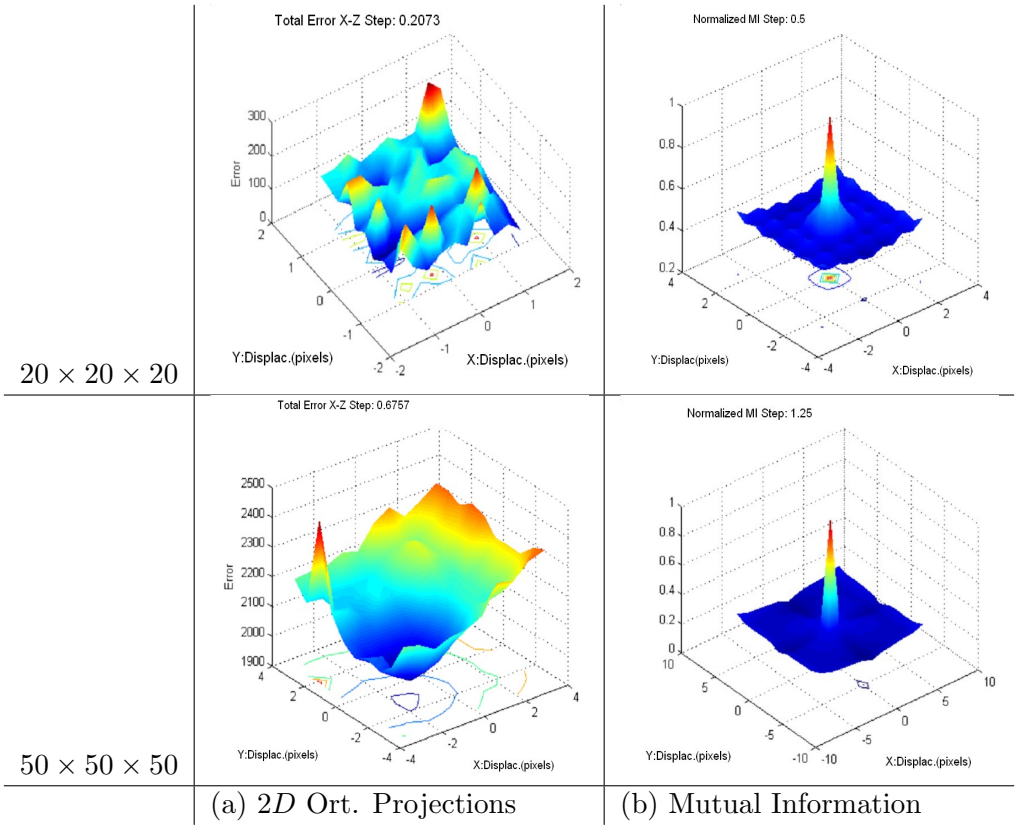

Figure 7.12: Multi-resolution cost functions for X-Z translation with different steps

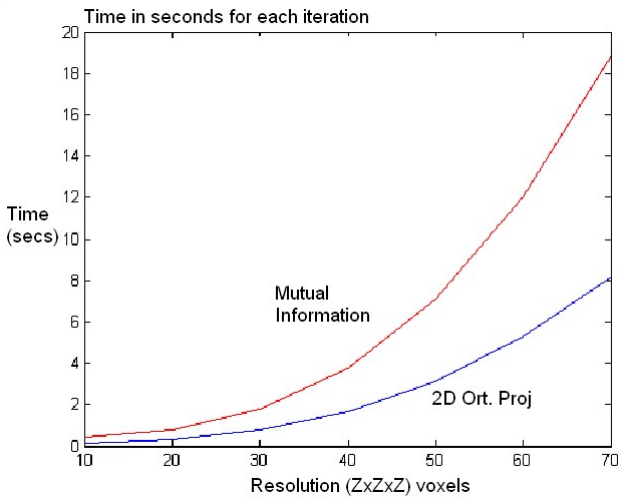

Figure 7.13: Iteration computation time for both registration methods taking into account the volume dimensions (Linear interpolation)

7.3.3 Summary

The cost functions for the developed $2D$ orthogonal projections show peaks. This is due to the detection of two circles by the Hough transform. This fact make the optimization process more difficult. They also show local minima surrounding the best solution. The computation time is proportional to the number of pixels in the projections. Therefore, a better evaluation of final accuracy versus computation time should be made in a faster implementation.

MI shows a clear maximum in a broad range of rotation angles and translations. The computation time depends on the number of the volume voxels. It could converge to the solution with less mutual information between the two volumes. Finally, MI is a robust method that can be applied.

7.4 Segmentation

According to section 4, two region-based segmentation methods are applied. The MR volume should be segmented. The results, taking into account the threshold value applied, the computation time, and the validity of the segmented technique, are shown in tables 7.3 and 7.4.

	Seeded reg. growing	
Threshold	Time(sec)	Result
0.1	5.8980	Non-Acceptable
0.3	6.1090	Acceptable
0.5	6.5090	Non-Acceptable
0.7	4.7670	Non-Acceptable
0.9	4.2060	Non-Acceptable

Table 7.3: Segmentation results for seeded region growing

	Region merging		
Threshold	Regions	Time(sec)	Result
0.1	9	274.1040	Non-Acceptable
0.3	3	276.9180	Non-Acceptable
0.5	2	276.0670	Non-Acceptable
0.7	2	275.7660	Non-Acceptable
0.9	2	276.5670	Non-Acceptable

Table 7.4: Segmentation results for region merging

For each method the change of the threshold value does not change significantly the segmentation time. The mean values for computation time can be seen in table 7.5. The advantage of seeded region growing is the low computation time and the convergence

to the desired solution. Disadvantages concern the location of the seeds requiring the knowledge of the operator. Region merging is automatic but the computation time and the uncertain convergence to the solution are its main disadvantages. In this work only region growing gives the appropriate solution with a threshold of 0.3. Further details for both segmentation methods and various thresholds are discussed in appendix B. In figure 7.14, representative slices for the segmented volume can be seen. Air corresponds to blue color, activity to red, and water to yellow. The number of assigned voxels is shown in figure 7.15. A total amount of 1756 voxels is non-assigned. These voxels correspond to the tubes filled with activity. Since none seed is located in the external markers, all this voxels should be labeled in order to get the attenuation map. Therefore these are assigned as activity.

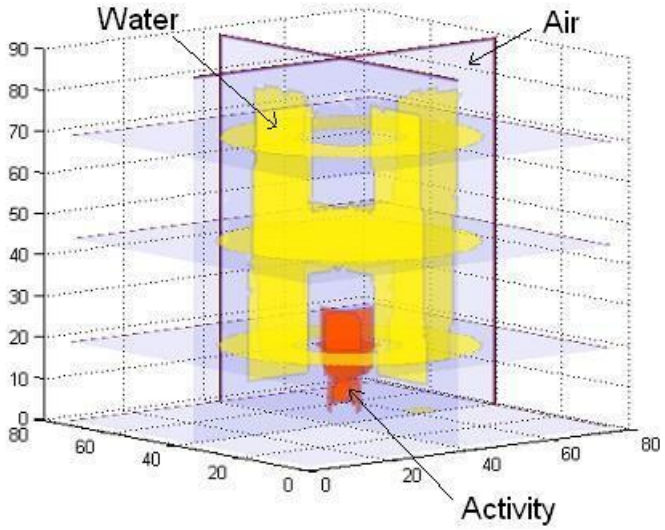

Figure 7.14: Segmented MR volume

7.5 Attenuation Map

The MR volume is segmented. Then the attenuation map can be calculated translating each tissue to its attenuation coefficient. For each labeled voxel the intensity values are mapped to attenuation coefficients. According to table 2.1 air has an attenuation

Method	Time(sec)
SRG	≈ 5.4978
RM	≈ 275.8844

Table 7.5: Segmentation time for both segmentation methods: Seeded region growing and Region merging

coefficient of 0.00010498 cm^{-1} and water has 0.09687 cm^{-1}. Activity can be consider to have the same attenuation coefficient as water. First, the registered MR attenuation map is developed. Subsequently it is interpolated to PET dimensions. Then new attenuation values are presented. These new values are mainly disposed between tissues. Therefore it does not pose a problem to make the new artifact-free reconstruction. An approximation to the PET attenuation map is developed. The representative slices of the volume are shown in figure 7.16. Yellow values in edges correspond to new attenuation values after interpolation. Thus the approximated attenuation map is blurred due to the low frequency response of interpolation.

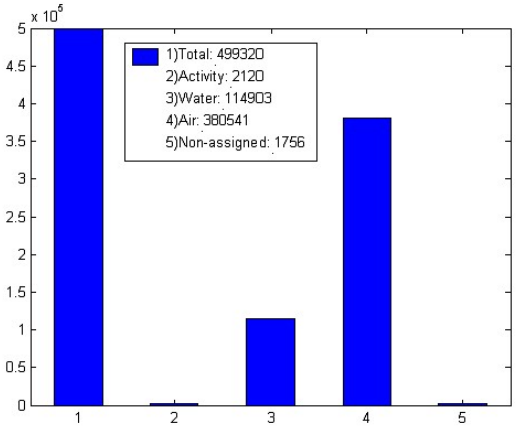

Figure 7.15: Labeled voxels on the segmented MR volume. (1) Total, (2) Activity, (3) Water, (4) Air, (5)Non-assigned

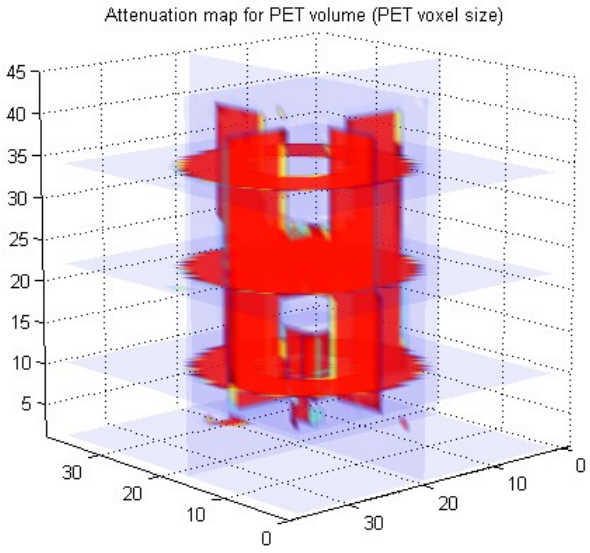

Figure 7.16: Interpretation of attenuation map for PET dimensions

Chapter 8

Conclusions

Here are presented the conclusions for experimental results of data acquisition as well as for algorithm results of registration and segmentation. The final evaluation of both aspects follows with the future work proposed to develop a definitive implementation of the attenuation correction algorithm based on MR data.

8.1 Results

- **Small animal phantom.** The initial problem related to the best disposition of the external markers has been widely studied depending on the results obtained from the different acquisition techniques. Although many configurations haven been proposed (see section 6), finally for the A-PET, a definitive disposition is suggested (see section 6.5). This disposition is good enough not only for our suggested 2D orthogonal projections registration method, but also it is helpful for mutual information registration. In conclusion, a small animal phantom with external markers for CT, MR and PET is developed and evaluated with different registration and segmentation methods.

- **MR imaging.** Time was mainly invested in MR since the new small animal PET scanner was going to come soon. Therefore improvements in MR images are developed. These improvements have the objective to obtain the best registration and segmentation results. The presence of noise that could affect the subsequent registration and segmentation is reduced. The distortion problem is also resolved. Furthermore a new protocol to obtain distortion free MR images is introduced and validated (see section 6.5).

- **Registration.** Testing the registration methods proposed in this project (see section 7), enough information is obtained about $2D$ ort. projections and MI methods. It is shown that PET/MR registration is possible by attaching external markers. For $2D$ ort. projections the convergence depends heavily on the shape of the markers used, and this configuration makes possible the validation with a model of the markers disposition. MI is valid to register the simulated functional PET image corresponding with a MR image.

- **Segmentation.** Clearly the 3D treatment that involves this work requires region based segmentation techniques to obtain the best performance. Despite only two segmentation methods have been applied, seeded region growing is found to be useful to acquire the attenuation map. As supervision is required, it is always desirable to check the validity in the first steps of the attenuation map developing.

8.2 Future Work

Clearly the straightforward implementation in MATLAB of registration and segmentation methods is not enough to satisfy the speed and accuracy requirements. The next steps are proposed:

- The convergence of $2D$ orthogonal projections registration method should be tested by using a faster implementation. It should be tested also with real and synthetic data.

- In a next step measurements and their registration should be considered with respect to a mouse. Then the accuracy of both registration methods can be compared.

- The arrival of the new small animal PET scanner opens new fields to investigate. Therefore new data sets should be tested to exploit all its characteristics. Moreover new activity concentration values located in the small receptacle and in the external markers can give different contrasts.

- Assuming correctly registered data, the segmentation and attenuation map should be refined and validated. The last experiment in A-PET/MR has provided a data set good enough to test new registration and segmentation methods. Anyway, new sources of distortion can be possible in the new scanner.

- Hybrid segmentation advanced methods can be proposed to combine other features. Other suggestion can be the direct identification of tissues based on the proton density of MR data.

Appendix A

Parameter Space Evaluation

In this appendix are shown the representative cost functions that provide an idea if the optimization process can reach the solution. All the cost functions correspond to the error evaluation of two parameters (the total number of parameters is six: three rotations and three translations). It takes into account that the function should be monotonous in a region surrounding the correct solution. Therefore a robustness measure of the algorithms can be obtained.

A.1 2D Orthogonal Projections

For 2D orthogonal projections translations in the X-Y axis from -5 to 5 pixels are represented (see figures A.1 and A.2). Rotations for the angles ϕ-γ from $-3°$ to $3°$ are shown (see figures A.3 and A.4). This variation is represented for the error of each projection and the total error. Taking into account the pixel size, a displacement of 1 pixel correspond to 0.5 mm. The step size used is 0.5 pixels for translations and 0.5° for rotations. A more accurate representation in the region of convergence of the cost functions are shown for translation and rotation with a step size of 0.25 pixels and 0.25°, respectively. The cost functions are represented for the non-registered data sets.

A.2 Mutual Information

The general shape of cost functions for Mutual Information are well-known. Anyway these are represented in order to check various parameters as the effect of interpolation methods and multi-resolution techniques. The cost functions represented are for the registered data sets. To minimize the computation time the dimensions are minimized to $40 \times 40 \times 40$. Translations in the X-Y axis from -5 to 5 pixels with a step size of 1 pixel are obtained (see figures A.5 and A.6). Rotations for the angles ϕ-γ from $-5°$ to $5°$ are shown (see figures A.7 and A.8). A more accurate representation in the region of convergence of the cost functions are shown for translation and rotation with a step size of 0.2 pixels and 0.2°, respectively.

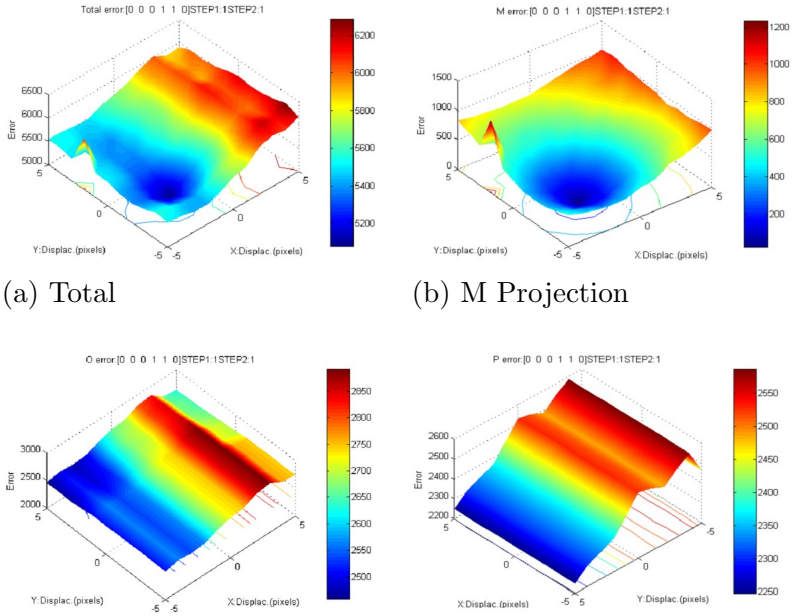

(a) Total (b) M Projection

(c) O Projection (d) P Projection

Figure A.1: Cost functions for translation in the X-Y axis from −5 to 5 pixels, step 1 pixel (2D)

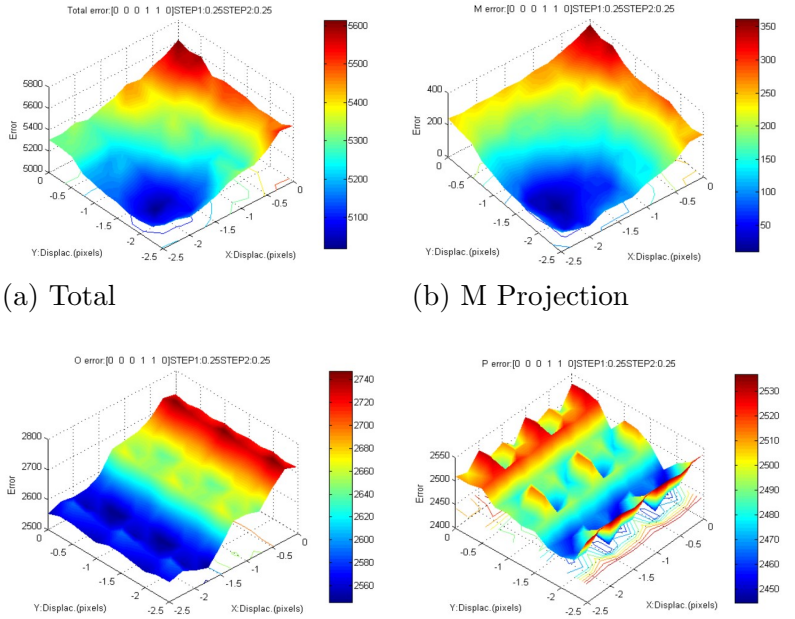

(a) Total (b) M Projection

(c) O Projection (d) P Projection

Figure A.2: Cost functions for translation in the X-Y axis in the region of interest, step 0.25 pixels (2D)

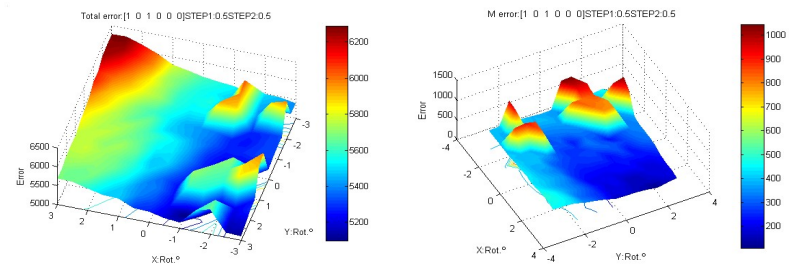

(a) Total (b) M Projection

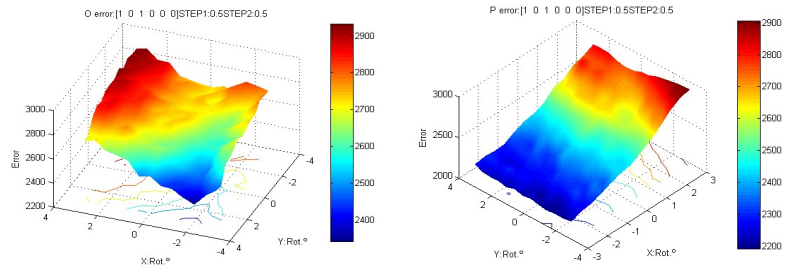

(c) O Projection (d) P Projection

Figure A.3: Cost functions for the angles ϕ-γ from $-3°$ to $3°$ pixels, step $0.5°$ (2D)

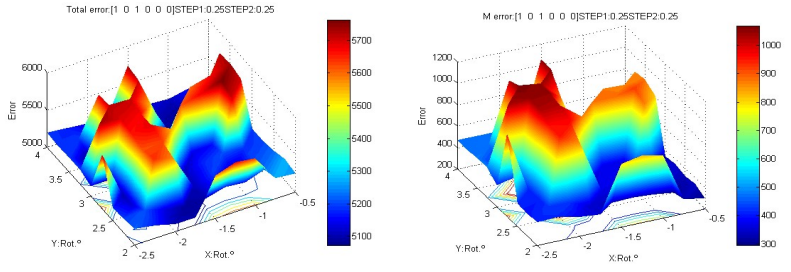

(a) Total (b) M Projection

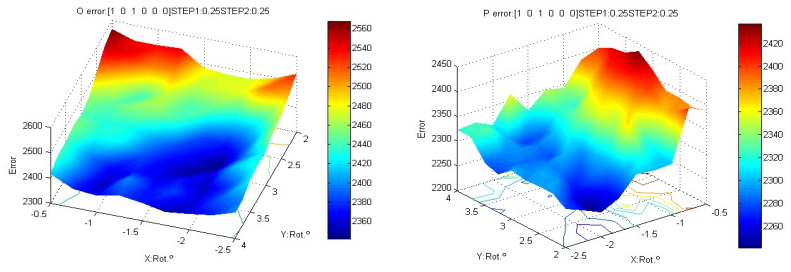

(c) O Projection (d) P Projection

Figure A.4: Cost functions for the angles ϕ-γ in the region of interest, step $0.25°$ (2D)

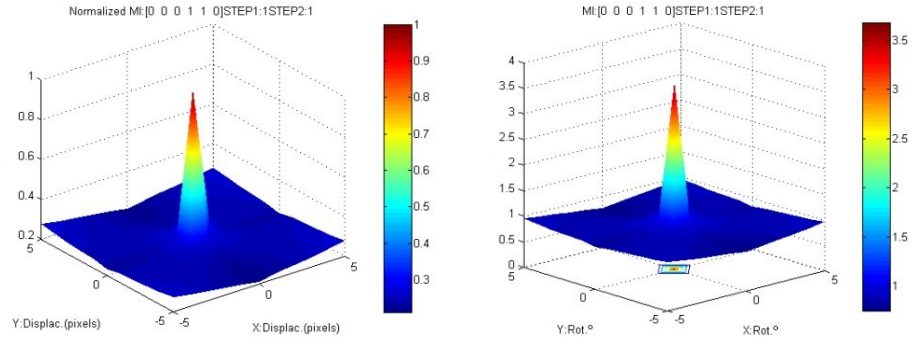

(a) NMI (b) MI

Figure A.5: Cost functions for translation in the X-Y axis from −5 to 5 pixels, step 1 pixel (MI)

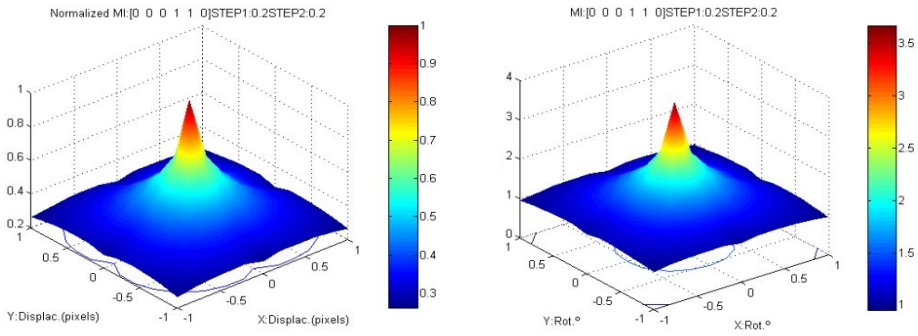

(a) NMI (b) MI

Figure A.6: Cost functions for translation in the X-Y axis in the region of interest, step 0.2 pixels (MI)

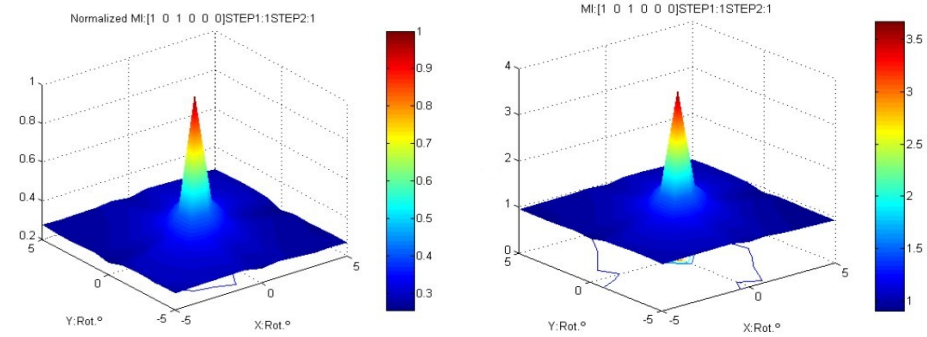

(a) NMI (b) MI

Figure A.7: Cost functions for the angles ϕ-γ from $-3°$ to $3°$ pixels, step $0.5°$ (MI)

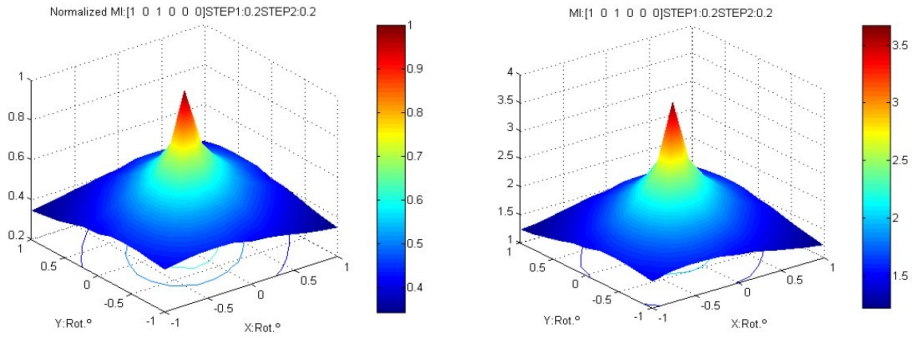

(a) NMI (b) MI

Figure A.8: Cost functions for the angles ϕ-γ in the region of interest, step 0.2° (MI)

Appendix B

Segmentation Results

Observing the different results of segmented regions in representative slices of the MR volume, the convenience of deciding one appropriate segmentation method can be made visually.

B.1 Seeded Region Growing

After visual inspection three seeds are located in certain positions in order that the algorithm could converge to the solution. For the small receptacle filled with activity one seed is located. In the big receptacle filled with water another one is located. Finally one more is needed to segment the air. Representative slices for MR containing the three different tissues show that the results vary according to the threshold value. For threshold values higher than 0.3 the segmentation results are not valid. This is because voxels belonging to different tissues are assigned to the same segmentation class. See figures B.1, B.2, B.3, B.4 and B.5.

B.2 Region Merging

It determines in an automated manner the different regions to segment. For the threshold value 0.1 nine regions are segmented. For the threshold value 0.3 three regions are segmented, this is the more accurate representation. Careful visual inspection of figure B.7 shows that the three segmented regions do not correspond spatially to the required tissues. One of these regions is assigned to the middle between the other two tissues. For threshold values higher than 0.3 only two regions are segmented. See figures B.6, B.7, B.8, B.9 and B.10.

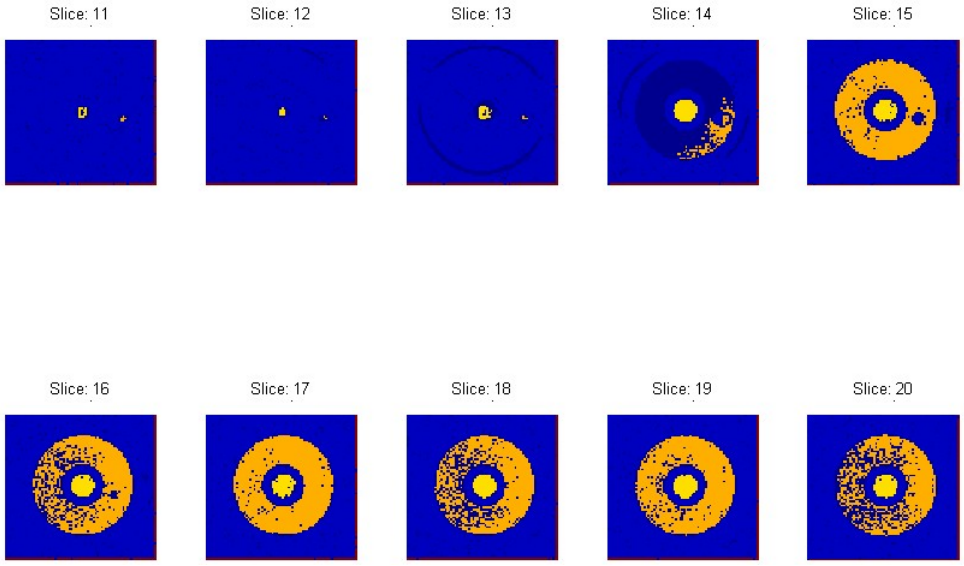

Figure B.1: Segmentation result for a threshold value 0.1 (SRG)

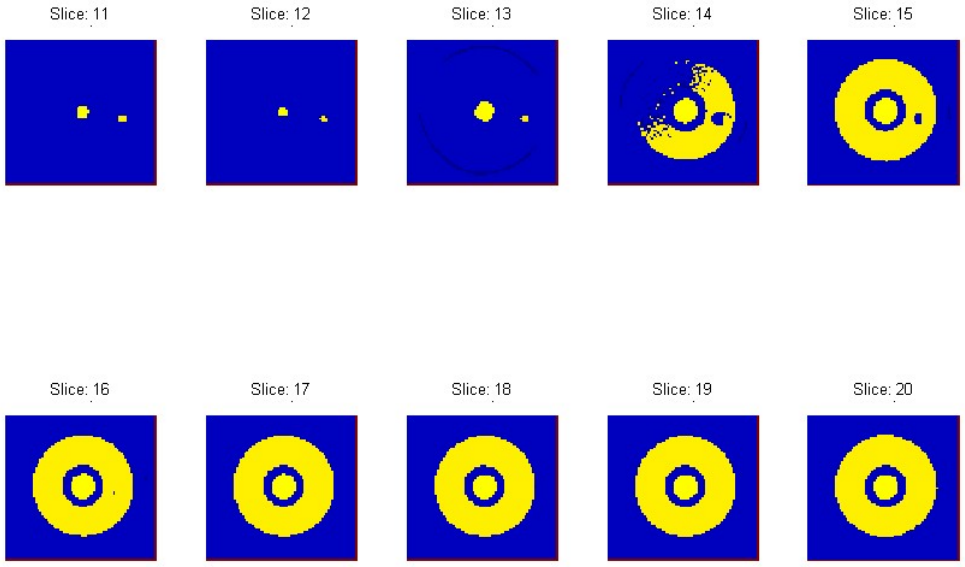

Figure B.2: Segmentation result for a threshold value 0.3 (SRG)

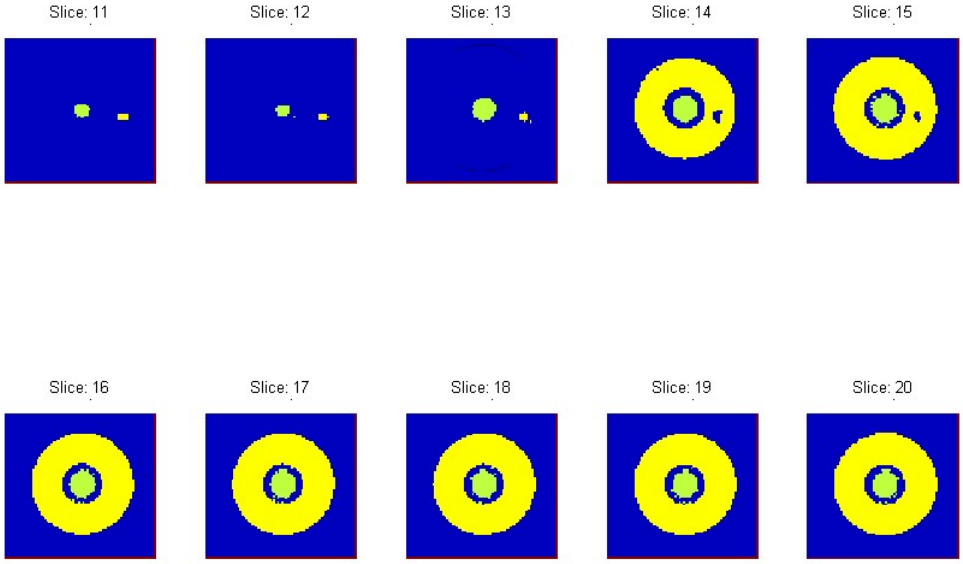

Figure B.3: Segmentation result for a threshold value 0.5 (SRG)

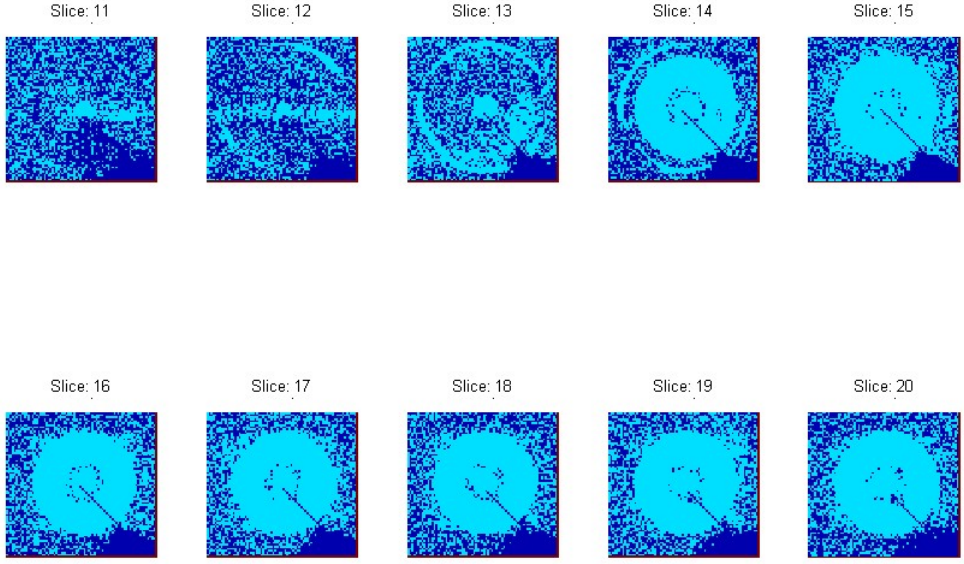

Figure B.4: Segmentation result for a threshold value 0.7 (SRG)

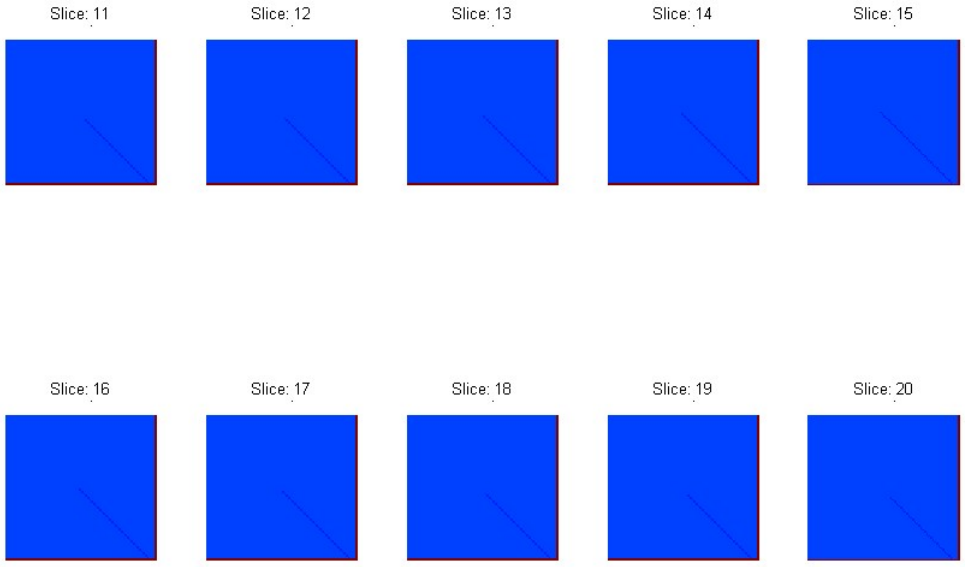

Figure B.5: Segmentation result for a threshold value 0.9 (SRG)

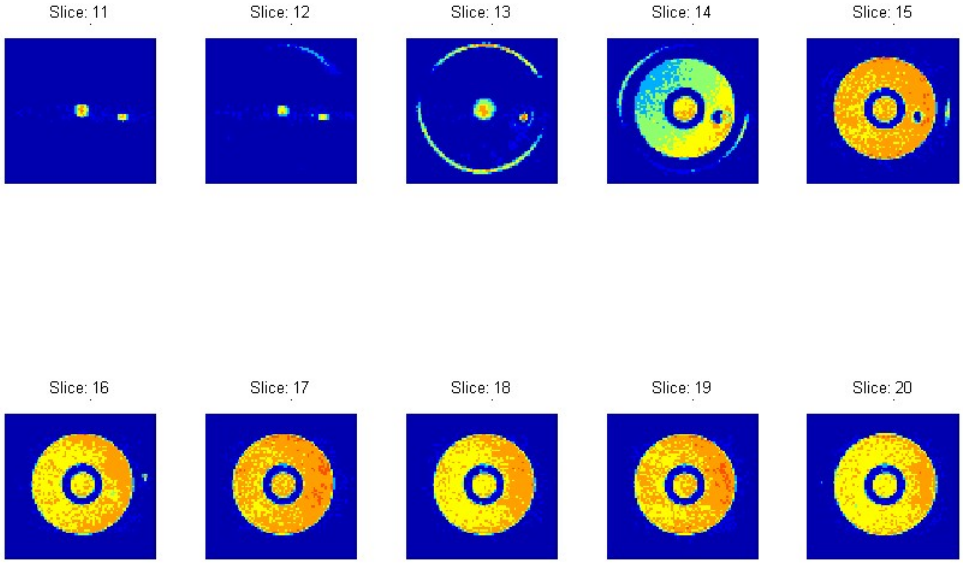

Figure B.6: Segmentation result for a threshold value 0.1 (RM)

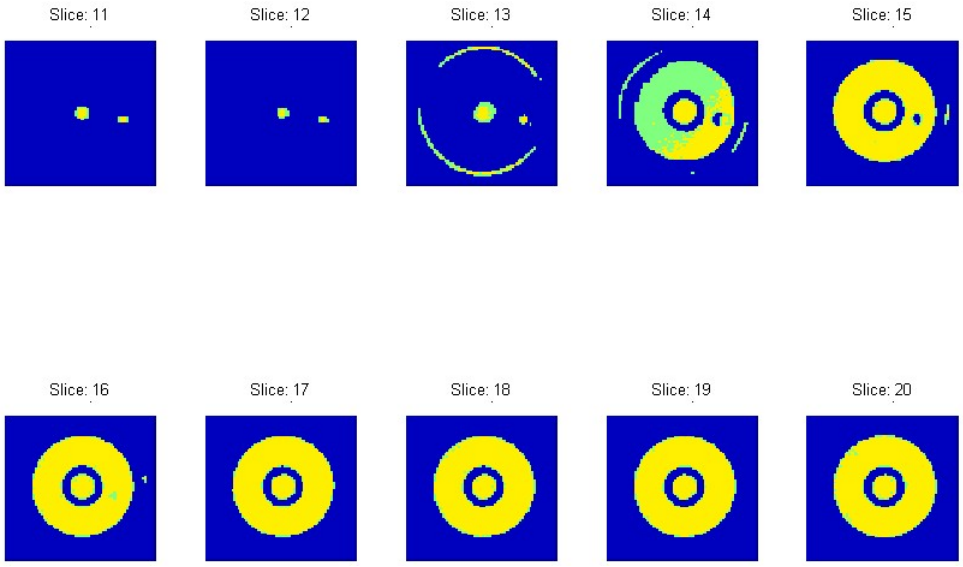

Figure B.7: Segmentation result for a threshold value 0.3 (RM)

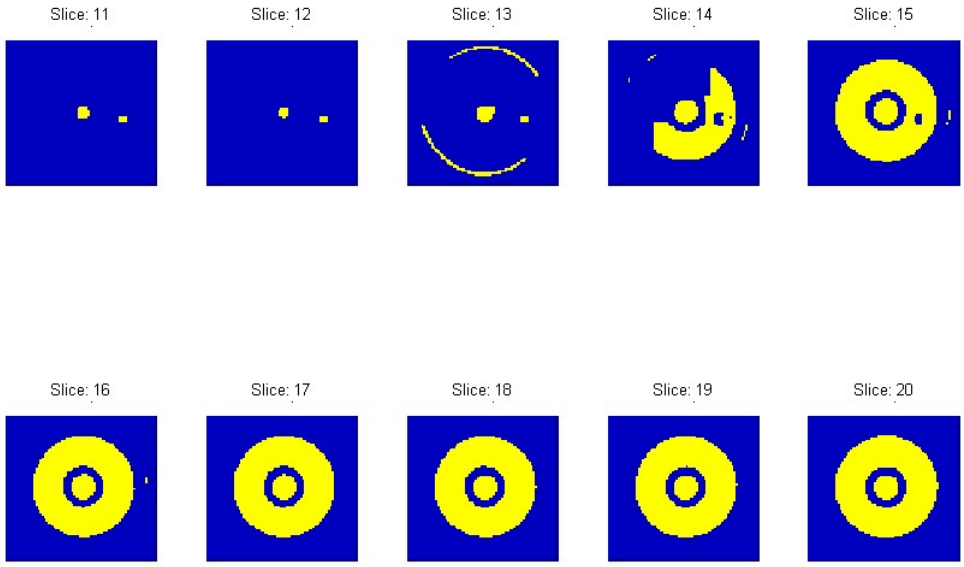

Figure B.8: Segmentation result for a threshold value 0.5 (RM)

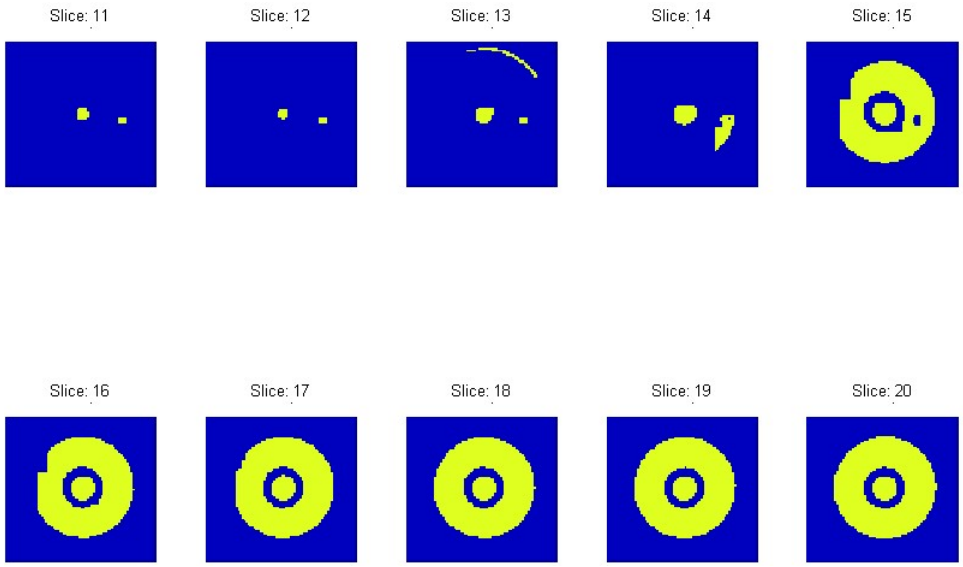

Figure B.9: Segmentation result for a threshold value 0.7 (RM)

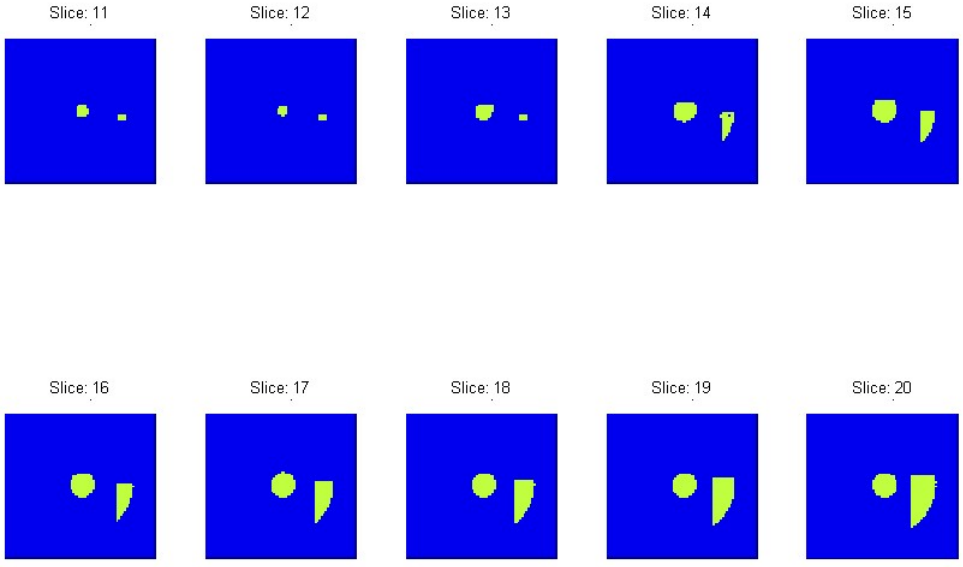

Figure B.10: Segmentation result for a threshold value 0.9 (RM)

Appendix C

Glossary

Artifact. Something artificial that does not reflect normal anatomy or pathology, not usually found in the body

Attenuation map. Image that contains attenuation values for each voxel

CT. Computed Tomography. A radiographic technique that obtains cross-sectional images by using a computer to assimilate multiple X-ray images

DICOM. Digital Imaging and Communications in Medicine. It is a standard that facilitates interoperability of medical imaging equipment

DT. Distance Transform. It maps binary images to distance values

FOV. Field of view. Region that can be treated for an object in imaging techniques

MADPET. Munich Avalanche Diodes PET. It is a small animal PET developed in the Nuklearmedizinische Klinik Klinikum rechts der Isar

MI. Mutual Information. A information theory measure developed by Shannon

MIP. Maximum Intensity Projection. A visualization technique widely used in medicine

MR. Magnetic Resonance. An imaging technique that uses the influence of a magnet to polarize hydrogen atoms in the tissues. Then it monitors the internal structures of the body

MRI. Magnetic Resonance Imaging

NIST. National Institute of Standards and Technology. Non-regulatory agency that develops standards and technology to enhance productivity and facilitate trade

PET. Positron Emission Tomography. A specialized research imaging technique using short lived radioactive substances, usually made with a cyclotron. It is sensitive in picking up active tumors tissues

Registration. Process of obtaining the transformation parameters to match two modal-

ity images

Segmentation. Process of recognizing different regions in images by distinguishing objects from background

Tracer. An element or compound containing atoms that can be distinguished from their normal counterparts by physical means (e.g. radioactivity) and can be used to follow the metabolism of the normal substances

SNR. Signal to Noise Ratio. Measure of signal strength relative to background noise presented in a signal

SLS. Sidelobe Suppresion. Relation of the second lobe elimination in power diagrams. It is usually expressed in dB

SRG. Seeded region growing. Region-based segmentation method that requires the location of seeds in the tissues to segment

Bibliography

[1] Allan M Cormack and Godfrey Newbold Hounsfield. *The 1979 Nobel Prize in Physiology or Medicine*. http://www.nobel.se/medicine/laureates/1979/press.html, 2003.

[2] Finn Arup Nielsen. *Bibliography on Image Registration*. Neurobiology Research Unit, Rigshospitalet and Informatics and Mathematical Modelling Technical University of Denmark, 2004.

[3] J. B. Antoine Maintz and Max A. Viergever. *An Overview of Medical Image Registration Methods*. 2001.

[4] Brian F. Hutton et al. *Image registration: an essential tool for nuclear medicine*. European Journal of Nuclear Medicine Vol. 29, No. 4, April, 2002.

[5] Derek L. G. Hill, Philipp G. Batchelor, Mark Holden, and David J. Hawkes. *Medical image registration*. Institute of Physics, 2001.

[6] L. P. Clarke et al. *MRI Segmentation: Methods and Applications*. Magnetic Resonance Imaging, Vol. 13, No. 3, pp. 343-368, 1995.

[7] N. Nikolaidis and Ioannis Pitas. *3-D Image Processing Algorithms*. Wiley-Interscience, 23 October, 2000.

[8] P.E. Kinahan, D. W. Townsend, T. Beyer, and D. Sashin. *Attenuation correction for a combined 3D PET/CT scanner*. 1999.

[9] Paul E. Kinahan, Bruce H. Hasegawa, and Thomas Beyer. *X-Ray-Based Attenuation Correction for Positron Emission Tomography/Computed Tomography Scanners*. Seminars in Nuclear Medicine, Vol XXXIII, No. 3, July, 2003.

[10] Habib Zaidi, Marie-Lousie Montandon, and Daniel O. Slosman. *Magnetic resonance imaging-guided attenuation and scatter corrections in three-dimensional brain positron emission tomography*. Medical Physics, Vol. 30, No. 5, May, 2003.

[11] Randal Slates et al. *Design of a Small Animal MR Compatible PET Scanner*. IEEE Transactions on Nuclear Science, Vol. 46, No. 3, June, 1999.

[12] Sibylle Ziegler et al. *A prototype high-resolution animal positron tomograph with avalanche photodiode arrays and LSO crystals*. European Journal of Nuclear Medicine Vol.28, No.2, February, 2001.

[13] Rasmus M. Birn, Kathleen M. Donahue, and Peter A. Bandettini. *Magnetic Resonance Imaging: Principles, Pulse Sequences and Functional Imaging.* Biophysics Research Institute, Medical College of Wisconsin, Volume 1, Chapter 9.

[14] Catherine Westbrook and Carolyn Kaut. *MRI in practice.* Blackwell Publishing, 1998.

[15] John M. Ollinger and Jeffrey A. Fessler. *Positron Emission Tomography.* IEEE Signal Processing Magazine, 14(1):43-55, January, 1997.

[16] Peter E. Valk, Dale L. Bailey, David W. Townsend, and Michael N. Maisey. *Positron Emission Tomography.* Springer, 2003.

[17] Richard M. Leahy and Jinyi Qi. *Statistical approaches in quantitative positron emission tomography.* Statistics and Computing 10, 147-165, 2000.

[18] Richard Hartley and Andrew Zisserman. *Multiple View Geometry in Computer Vision.* Cambridge University Press, 2000.

[19] Wolfgnag Wein. *Intensity Based Rigid 2D-3D Registration Algorithms for Radiation Therapy.* Diplomarbeit TUM, 2004.

[20] Jiahui Pan. *Image Interpolation using Spline Curves.* Dept. of Mechanical Engineering MEC572 term paper, 2003.

[21] Thomas M. Lehmann, Claudia Gögner, and Klaus Spitzer. *Survey: Interpolation Methods in Medical Image Processing.* IEEE Transactions on Medical Imaging, vol. 18, No. 11, 1999.

[22] Erik H. W. Meijering. *Spline Interpolation in Medical Imaging: Comparison with other convolution-based approaches.* Images Sciences Institute, University Medical Center Utrecht.

[23] Erik H. W. Meijering, Wiro J. Niessen, Josien P. W. Pluim, and Max A. Viergever. *Quantitative Comparison of Sinc-Approximating Kernels for Medical Image Interpolation.* Images Sciences Institute, University Medical Center Utrecht.

[24] Yi Sun and Dennis L. Parker. *Performance Analysis of Maximum Intensity Projection Algorithm for Display of MRA Images.* IEEE Transactions on medical Imaging, Vol. 18, No. 12, December, 1999.

[25] Ho-Ming Chan and Albert C. S. Chung. *Efficient 3D-3D Vascular Registration Based on Multiple Orthogonal 2D Projections.* Dept. of Computer Science, Hong Kong University of Science and Technology, HK.

[26] Rui Gang, Albert C. S. Chung, Wilbur C. K. Wong, and Simon C. H. Yu. *Vascular Segmentation in Three-Dimensional Rotational Angiography Based on Maximum Intensity Projections.* Dept. of Computer Science, the University of Science and Technology, HK.

[27] J. F. Canny. *Finding edges and lines in images*. Master's thesis, MIT. AI Lab TR-720, 1983.

[28] J. F. Canny. *A computational approach to edge detection*. IEEE Trans. Pattern Analysis and Machine Intelligence, 8:679-698, 1986.

[29] D. Marr and E. C. Hildreth. *Theory of edge detection*. Proceedings of the Royal Society, London B, 207: 187-217, 1980.

[30] Glaucius Décio Duarte. *Uso da Transformada de Hough na Detecção de Círculos em Imagens Digitais*.

[31] Yi Pan Keqin Li and Mounir Hamdi. *An Improved Constant-Time Algorithm for Computing the Radon and Hough Transforms on a Reconfigurable Mesh*. IEEE Transactions on Systems, Man and Cybernetics, Vol. 29 No. 4 July, 1999.

[32] Olivier Cuisenaire. *Distance Transformations: Fast algorithms and Applications to Medical Image Processing*. Ph. D. Thesis, Université Catholique de Louvain, Belgium, October, 1999.

[33] C. E. Shannon. *A Mathematical Theory of Communication*. The Bell System Technical Journal Vol.27 pp. 379-423, 623-656, JUly, October, 1948.

[34] Josien P. W. Pluim, J. B. Antoine Maintz, and Max A. Viergever. *Image registration by maximization of combined mutual information and gradient information*. IEEE Transactions on Medical Imaging, 19(8), 2000.

[35] Frederik Maes, Dirk Vandermeulen, and Paul Suetens. *Medical Image Registration using Mutual Information*. Proceedings of the IEEE, Vol. 91, No. 10, October, 2003.

[36] Josien P. W. Pluim, J. B. Antoine Maintz, and Max A. Viergever. *Mutual information based registration of medical images: a survey*. IEEE Transactions on Medical Imaging, Vol. XX, No. Y, 2003.

[37] Jeffrey C. Lagarias, James A. Reeds Margaret, H. Wright, and Paul E. Wright. *Convergence Properties of the Nelder-Mead Simplex Method in Low Dimensions*. SIAM Journal of Optimization, Vol. 9 Number 1, pp. 112-147, 1998.

[38] R. Adams and L. Bischof. *Seeded region growing*. IEEE Trans. Pattern Anal. Mach. Intelligence, 16(6):641-647, 1994.

[39] Yingli Lu, Tianzi Jiang, and Yufeng Zang. *Region growing method for the analysis of functional MRI*. NeuroImage 20 455-465, 2003.

[40] Zheng Lin, Jesse Jin, and Hughes Talbot. *Unseeded region growing for 3D image segmentation*. Conferences in Research and Practice in Information Technology, Vol. 2, December, 2000.

[41] Marc Van Droogenbroeck and Hugues Talbot. *Segmentation by Adaptative Prediction and Region Merging.* VIIth Digital Image Computing: Techniques and Applications, Sydney, 10-12 Dec., 2003.

[42] Habib Zaidi and Bruce Hasegawa. *Determination of the Attenuation Map in Emission Tomography.* Journal Nuclear Medicine, 44:291-315, May, 2002.